



# Vertical profile of $\delta^{18}\text{O}^{\text{OO}}$ from the middle stratosphere to lower mesosphere from SMILES spectra

T. O. Sato<sup>1,2</sup>, H. Sagawa<sup>2</sup>, N. Yoshida<sup>1,3</sup>, and Y. Kasai<sup>2,1</sup>

<sup>1</sup>Tokyo Institute of Technology, 4259 Nagatsuta, Midori, Yokohama, Kanagawa 226-8503, Japan

<sup>2</sup>National Institute of Information and Communications Technology, 4-2-1 Nukui-kitamachi, Koganei, Tokyo 184-8795, Japan

<sup>3</sup>Earth-Life Science Institute, Tokyo Institute of Technology, 2-12-1 Ookayama, Meguro, Tokyo 152-8551, Japan

Correspondence to: Y. Kasai (ykasai@nict.go.jp)

Received: 22 August 2013 – Published in Atmos. Meas. Tech. Discuss.: 15 October 2013

Revised: 19 February 2014 – Accepted: 19 February 2014 – Published: 10 April 2014

**Abstract.** Ozone is known to have large oxygen isotopic enrichments of about 10 % in the middle stratosphere; however, there have been no reports of ozone isotopic enrichments above the middle stratosphere. We derived an enrichment  $\delta^{18}\text{O}^{\text{OO}}$  in the stratosphere and the lower mesosphere from observations of the Superconducting Submillimeter-Wave Limb-Emission Sounder (SMILES) onboard the International Space Station (ISS) using a retrieval algorithm optimized for the isotopic ratio. The retrieval algorithm includes (i) an a priori covariance matrix constrained by oxygen isotopic ratios in ozone, (ii) an optimization of spectral windows for ozone isotopomers and isotopologues, and (iii) common tangent height information for all windows. The  $\delta^{18}\text{O}^{\text{OO}}$  by averaging the SMILES measurements at the latitude range of 20 to 40° N from February to March in 2010 with solar zenith angle < 80° was 13 % (at 32 km) with the systematic error of about 5 %. SMILES and past measurements were in good agreement, with  $\delta^{18}\text{O}^{\text{OO}}$  increasing with altitude between 30 and 40 km. The vertical profile of  $\delta^{18}\text{O}^{\text{OO}}$  obtained in this study showed an increase and a decrease with altitude in the stratosphere and mesosphere, respectively. The  $\delta^{18}\text{O}^{\text{OO}}$  peak, 18 %, is found at the stratopause. The  $\delta^{18}\text{O}^{\text{OO}}$  has a positive correlation with temperature in the range of 220–255 K, indicating that temperature can be a dominant factor to control the vertical profile of  $\delta^{18}\text{O}^{\text{OO}}$  in the stratosphere and mesosphere. This is the first report of the observation of  $\delta^{18}\text{O}^{\text{OO}}$  over a wide altitude range extending from the stratosphere to the mesosphere (28–57 km).

## 1 Introduction

Ozone plays an important role in the Earth's atmosphere, and has a pronounced oxygen isotopic enrichment and anomaly. Isotopic enrichment is defined as

$$\delta^m\text{O} = \left( \frac{m R_{\text{obs}}}{m R_{\text{std}}} - 1 \right) \times 100 (\%), \quad (1)$$

$$m R = \frac{[m\text{O}]}{[^{16}\text{O}]}, \quad (2)$$

where  $m$  is a mass of heavy oxygen (either 17 or 18). The oxygen isotopic ratio of standard mean ocean water (SMOW) is used as the standard  $R_{\text{std}}$  (SMOW –  $^{16}\text{O} : ^{17}\text{O} : ^{18}\text{O} = 1 : 1/2700 : 1/500$ ) in this paper. Isotopic signature in atmospheric ozone affects a host of oxygen isotopic ratios in other trace constituents such as  $\text{CO}_2$  and  $\text{N}_2\text{O}$  (Lyons, 2001). Mauersberger (1981) reported the first measurement of ozone isotopic enrichment using a balloon-based mass spectrometer that showed greater than 40 % enrichment in stratospheric 18 heavy ozone ( $^{50}\text{O}_3$ ), which is larger than expected values. Although the measurement performed by Mauersberger (1981) is mentioned to be reanalyzed (Mauersberger et al., 2001), the first measurement in 1981 did trigger subsequent measurements of oxygen isotopic ratio in stratospheric ozone.

Measurements using a mass spectrometer have the advantage of high accuracy (0.01–0.1 %), but it is hard to distinguish molecules that have the same mass with different isotopomers such as  $^{18}\text{O}^{\text{OO}}$  (asymmetric-18 ozone) and  $\text{O}^{18}\text{OO}$  (symmetric-18 ozone). Using spectroscopic techniques, asymmetric and symmetric isotopomers are

separately observed. Irion et al. (1996) observed oxygen isotopic enrichments of  $^{18}\text{O}$ OOO and  $\text{O}^{18}\text{OO}$  in the middle stratosphere using space-based solar occultation spectra by the Atmospheric Trace Molecule Spectroscopy (ATMOS) experiment. Their globally averaged enrichments between 24 and 41 km were  $15 \pm 6\%$  and  $10 \pm 7\%$  for  $^{18}\text{O}$ OOO and  $\text{O}^{18}\text{OO}$ , respectively. This inhomogeneous isotopic enrichment between  $^{18}\text{O}$ OOO and  $\text{O}^{18}\text{OO}$  was supported by the measurements using a balloon- and aircraft-based Fourier transform infrared (FTIR) spectrometer by Johnson et al. (2000) and Haverd et al. (2005). The measured vertical profiles of isotopic enrichments in  $^{18}\text{O}$ OOO and  $\text{O}^{18}\text{OO}$  showed an increase with altitude in the middle stratosphere (20–40 km). Krankowsky et al. (2007) precisely measured  $\delta^{18}\text{O}$  in bulk ozone ( $^{50}\text{O}_3$ ) using a sample collection technique, and confirmed an increasing of ozone isotopic enrichment with altitude from 7 to 12 % at 21 and 34 km, respectively. They also showed a latitudinal variation of  $\delta^{18}\text{O}$  that was more pronounced near the Equator than in the middle latitude regions, although the observations had been performed in different years.

Measured ozone isotopic enrichment is explained by isotopic fractionation due to the three-body formation reaction (about 10 % of enrichment):



where  $\delta^{18}\text{O}$  increases with temperature (e.g., Morton et al., 1990; Hathorn and Marcus, 1999; Gao and Marcus, 2001). This temperature dependence is relatively consistent with the behavior in the observed ozone isotopic enrichment. There is another contribution from the photolysis of ozone (about 3 % of enrichment),



especially above 30 km. Liang et al. (2006) separately calculated vertical profiles of ozone isotopic enrichments due to the formation process and photolysis using the 1-D Caltech/JPL KINETICS model. The  $\delta^{18}\text{O}$ OOO values estimated by this model were in good agreement with the measurements in the lower to middle stratosphere (20–35 km) but were underestimated at higher altitudes (35–40 km). The discrepancy between the measurements and the model is principally because of a lack of measurements of ozone isotopic enrichment above 40 km (in the upper stratosphere and the mesosphere). Hence, more observations of ozone isotopic enrichment at the higher altitudes is needed.

The Superconducting Submillimeter-Wave Limb-Emission Sounder (SMILES) is an instrument that observes atmospheric submillimeter-wave emission using superconducting technology for radiation-receiving systems (Kikuchi et al., 2010). SMILES was launched and docked on the Japanese Experiment Module (JEM) of the International Space Station (ISS) in September 2009. The operation period was between 12 October 2009 and 21 April 2010.

SMILES has three observation frequency bands in the submillimeter-wave region (band A: 624.32–625.52 GHz; band B: 625.12–626.32 GHz; band C: 649.12–650.32 GHz). Two of the three bands are simultaneously observed by means of two acousto-optical spectrometers (AOSs), named AOS 1 and AOS 2, with a bandwidth of 1.2 GHz. The transitions of  $\text{O}_3$  (O means  $^{16}\text{O}$  hereafter),  $^{18}\text{O}$ OOO,  $\text{O}^{18}\text{OO}$ ,  $^{17}\text{O}$ OOO and  $\text{O}^{17}\text{OO}$  are located in the SMILES bands, although the intensity of the transition of  $\text{O}^{18}\text{OO}$  is quite small (see Fig. 1). SMILES provides low-noise spectra, enabling observations of weak emissions at high altitudes with good signal-to-noise (S/N) ratios. For a single spectrum, the S/N ratio of the  $^{18}\text{O}$ OOO transition at 649.137 GHz in band C is about 40 and 3 in the stratosphere and mesosphere, respectively. Vertical profiles of  $\text{O}_3$  concentrations were observed up to the upper mesosphere using SMILES observation data (Kasai et al., 2013). Prior to the launch of SMILES, Kasai et al. (2006) estimated the expected precision and accuracy of SMILES ozone isotopic enrichment observations. They reported a precision of a few percent over a  $10^\circ$  daily zonal mean profile and an accuracy of about 15 % for the enrichments for  $^{18}\text{O}$ OOO,  $^{17}\text{O}$ OOO and  $\text{O}^{17}\text{OO}$ . There have been many improvements in the SMILES measurements such as a spectral nonlinear gain calibration, retrieval algorithm and model parameters since the launch. SMILES has the ability to observe ozone isotopic enrichments in the middle stratosphere and higher.

In this study, we develop a retrieval algorithm optimized for ozone isotopic enrichments using SMILES observation data (described in Sect. 2). In Sect. 3, the error in  $\delta^{18}\text{O}$ OOO derived from the developed retrieval algorithm is estimated by a quantitative error analysis. We also compare the average  $\delta^{18}\text{O}$ OOO values in a latitude range of 20 to 40° N from February to March in 2010 during the daytime (solar zenith angle (SZA) < 80°) with past measurements. The  $\delta^{18}\text{O}$ OOO in the altitude region from the upper stratosphere to the lower mesosphere is discussed in Sect. 4. We report, for the first time, vertical profiles of  $\delta^{18}\text{O}$ OOO encompassing both the stratosphere and the mesosphere.

## 2 Development of retrieval algorithm

We developed the optimized retrieval algorithm for ozone isotopic ratio by SMILES (TOROROS). This algorithm is based on the SMILES NICT level 2 retrieval algorithm version 2.1.5 (called “V215” in this paper). The SMILES retrieval algorithm is based on the least-squares method with an a priori constraint (e.g., Rodgers, 2000). The forward model consists of a clear-sky radiative transfer model and numerical instrument models of SMILES. A detailed description for the version 2.X.X series of the SMILES NICT level 2 processing, including V215, can be found in Baron et al. (2011).

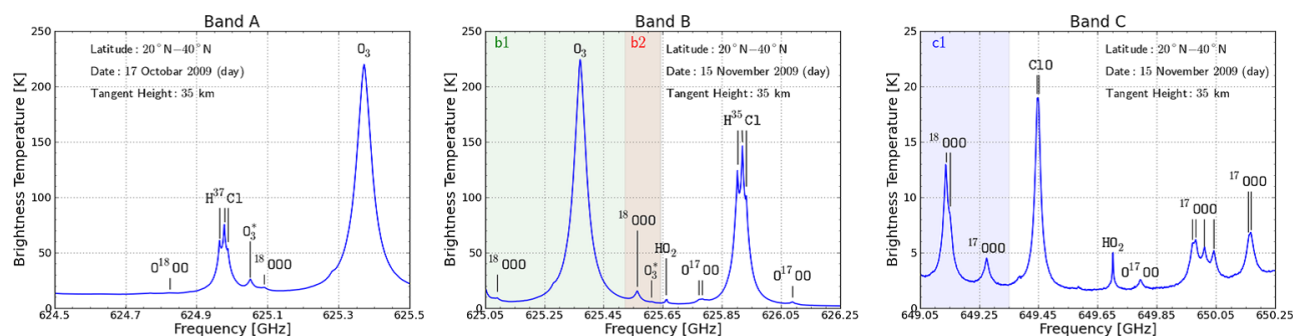


**Fig. 1.** SMILES observation spectra (level-1b version 008) of band A (left), band B (center) and band C (right). Fifty spectra were accumulated under the following conditions. Tangent height:  $35 \pm 2.5$  km. Latitude:  $20\text{--}40^\circ$  N. Time: daytime on 17 October (band A) and 15 November (bands B and C) in 2009. Green, red and blue shadings represent the b1, b2 and c1 frequency windows, respectively (see Table 1).

**Table 1.** Spectral windows of TOROROS.

Window/band	Frequency range	Target	Altitude range
b1 / band B	625.042–625.642 GHz	$\text{O}_3$	20–80 km
b2 / band B	625.522–625.642 GHz	$^{18}\text{O}^{16}\text{O}^{16}\text{O}$ , $\text{O}_3^*$	30–60 km
c1 / band C	649.000–649.350 GHz	$^{18}\text{O}^{16}\text{O}^{16}\text{O}$ , $^{17}\text{O}^{16}\text{O}^{16}\text{O}$	25–60 km
b0 / band B	625.042–625.642 GHz	Temperature	20–60 km

## 2.1 Level-1b spectrum and tangent height correction

We employed the level-1b (L1b) data version 008 released in 2012. This version updated a nonlinear gain calibration of spectrum brightness temperature (Ochiai et al., 2012a). As emphasized by Kasai et al. (2013), the nonlinearity issue was one of the biggest causes of error in the retrieval of the  $\text{O}_3$  VMR in the V215 retrieval processing. Tangent height information was also improved using auxiliary data acquired by the SMILES star tracker sensor and the Monitor of All-sky X-ray Image (MAXI) instrument (Ochiai et al., 2012b).

A tangent height offset was estimated by comparing the brightness temperatures observed by SMILES with those calculated by the forward model, described in Sect. 2.3, in the frequency range of 649.56 to 649.69 GHz. Intensities of the atmospheric molecular transitions in this frequency range are quite small: therefore, effects from atmospheric molecular radiations and their variations are minimized. The method of this bias estimation was not changed from V215 (see Sect. 3 of Baron et al., 2011, for further details). The tangent height bias offset was estimated to be about 2–3 km.

## 2.2 Window configuration

As mentioned in Sect. 1, only two of the three bands can be simultaneously observed. The AOSs assigned to bands B and C are fixed; in other words the observations of bands B and C are always performed by AOS 2 and AOS 1, respectively. Band A is observed by either AOS 1 or AOS 2. We used only

data of the observation from bands B and C for this study, so as not to cause any undesirable errors due to instrumental differences in the band configuration.

We set three spectral windows to retrieve the VMR of  $\text{O}_3$  and  $^{18}\text{O}^{16}\text{O}^{16}\text{O}$  in bands B and C, and one spectral window for the temperature (see Fig. 1 and Table 1). Setting windows with a small frequency range has the advantage of reducing contaminations from transitions of molecules different from the target. In the case of spectral lines of  $\text{O}_3$  and  $^{18}\text{O}^{16}\text{O}^{16}\text{O}$  in band B, the spectral intensity of  $\text{O}_3$  is much larger than that of  $^{18}\text{O}^{16}\text{O}^{16}\text{O}$ , and the  $^{18}\text{O}^{16}\text{O}^{16}\text{O}$  line is located at the wing slope of the  $\text{O}_3$  line. If their VMRs are simultaneously retrieved, a retrieval solution is converged to one that is optimized for  $\text{O}_3$  rather than  $^{18}\text{O}^{16}\text{O}^{16}\text{O}$ . Hence we set retrieval windows individually for  $\text{O}_3$  and  $^{18}\text{O}^{16}\text{O}^{16}\text{O}$  (window b1 and b2, respectively). The retrieval processes of the four windows were independent of each other to prevent any error propagation from window to window.

Window b1 in band B was set to retrieve  $\text{O}_3$  VMR using the transition at 625.371 GHz. The frequency range was between 625.042 and 625.642 GHz. Other parameters simultaneously retrieved were the VMRs of other molecules ( $^{18}\text{O}^{16}\text{O}^{16}\text{O}$ , ozone in the vibrational state  $\text{O}_3^*$ ,  $\text{H}_2\text{O}$ ,  $\text{HNO}_3$  and  $\text{HOCl}$ ), the frequency shift and a first-order polynomial representing a spectral baseline. The pressure and temperature profile was fixed to be the a priori (described in Sect. 2.4). The intervals of the retrieval altitude grid were 4 and 5 km at

altitudes below and above 30 km, respectively. This altitude grid was commonly applied for all the windows.

Two windows were set in bands B and C for  $^{18}\text{O}$ . Window b2 in band B retrieves  $^{18}\text{O}$  VMR using the transition at 625.564 GHz that is located at the wing of the  $\text{O}_3$  line at 625.371 GHz.  $\text{O}_3$  VMR was simultaneously retrieved to fit a spectral baseline. Window c1 in band C retrieves  $^{18}\text{O}$  VMR using the lines at 649.137 and 649.152 GHz.  $^{17}\text{O}$  VMR is also retrieved with the transition at 649.275 GHz in window c1. These transitions are isolated from other lines with large intensities. Frequency shifts and second-order polynomial baselines were also retrieved.

In window b0, the temperature was retrieved from the  $\text{O}_3$  line at 625.371 GHz. The frequency range and the retrieved parameters were the same as window b1. The temperature profile retrieved in window b0 is used for a discussion of temperature dependence of  $\delta^{18}\text{O}$ .

There are  $\text{O}^{18}\text{O}$  transitions at 624.505 and 624.825 GHz in band A, but unfortunately their intensities are too weak to retrieve  $\text{O}^{18}\text{O}$  VMR for the purpose of a discussion of isotopic ratio. Moreover, the transitions of  $\text{CH}_3\text{CN}$ , which are located quite close to the  $\text{O}^{18}\text{O}$  transitions, cause large contaminations. In this paper a retrieval of  $\text{O}^{18}\text{O}$  VMR is not discussed.

### 2.3 Forward model

We employed the V215 forward model ( $\mathcal{F}$ ) with the following improvements. Spectroscopic parameters are one of the largest error sources in the retrieval of  $\text{O}_3$  VMR for V215 (Kasai et al., 2013), and those of ozone isotopomers and isotopologues were updated based on the JPL catalog (Pickett et al., 1998), the HITRAN 2008 database (Rothman et al., 2009) and latest laboratory experiments (e.g., Drouin and Gamache, 2008). Table 2 summarizes the spectroscopic parameters of ozone isotopomers and isotopologues used in the windows b1, b2 and c1.

Instrument functions have been improved from those in V215 with respect to an antenna beam pattern ( $R_{\text{ANT}}$ ), a side-band separator (SBS) and an AOS response function.  $R_{\text{ANT}}$  was implemented with a two-step modification. First,  $R_{\text{ANT}}$  was integrated in the vertical direction considering SMILES' field of view. The atmosphere is assumed to be horizontally stratified and an integration is performed in the vertical direction. Second, considering a movement of the antenna over 0.5 s, which is the data integration time for one limb emission spectrum, the instantaneous antenna response pattern  $R_{\text{ANT}}$  was modified to represent the actual SMILES limb scan mechanism. A rejection rate of an image band ( $\beta_{\text{image}}$ ) was implemented considering the SBS characteristics. We employed the AOS response function improved by Mizobuchi et al. (2012). The AOS response function was obtained by fitting with three Gaussian functions. An accuracy of the fitting is better than that in the L1b data version 007. The error in the AOS response function used in TOROROS

was estimated to be about 5 % in full width at half maximum (FWHM), which is half of the previous version (10 %).

### 2.4 Inversion calculation

In the TOROROS algorithm, a solution of the retrieval state vector  $\mathbf{x}$  is determined by minimizing the following cost function  $\chi^2$ :

$$\chi^2 = (\mathbf{y} - \mathcal{F}(\mathbf{x}, \mathbf{b}))^T \mathbf{S}_y^{-1} (\mathbf{y} - \mathcal{F}(\mathbf{x}, \mathbf{b})) + (\mathbf{x} - \mathbf{x}_a)^T \mathbf{S}_x^{-1} (\mathbf{x} - \mathbf{x}_a). \quad (3)$$

$\mathbf{S}_y$  and  $\mathbf{S}_x$  are covariance matrices for measurement spectrum noise and an a priori state ( $\mathbf{x}_a$ ), respectively.  $\mathbf{S}_y$  is a diagonal matrix with elements  $(0.5 \text{ K})^2$ .  $\mathbf{x}_a$  of  $\text{O}_3$  VMR was taken from the Goddard Earth Observing System Model version 5.2 (GEOS-5) (Rienecker et al., 2008) at altitudes below 60 km, and the VMR value at 60 km was extended to 120 km. A priori VMR profiles of the other ozone isotopomers and isotopologues were calculated based on knowledge from past measurements of oxygen isotopic ratios in ozone. The  $^{18}\text{O}$  a priori VMR was calculated based on the  $\text{O}_3$  a priori VMR to follow 10 %  $\delta^{18}\text{O}$  against the SMOW standard for all altitudes. The  $\text{O}^{18}\text{O}$  a priori VMR was 5 %  $\delta\text{O}^{18}\text{O}$  following a statistical rule. The a priori VMRs of  $^{17}\text{O}$  and  $\text{O}^{17}\text{O}$  were calculated using the relationship of mass-dependent fractionation ( $\delta^{17}\text{O} = 0.515 \delta^{18}\text{O}$ ).

The pressure and temperature a priori profiles were taken from GEOS-5 and the Mass Spectrometer and Incoherent Scatter (MSIS) climatology (Hedin, 1991), as implemented in V215. The former profile was for the altitude region from the surface to 70 km and the latter was from 70 to 120 km. They were smoothly interpolated assuming a hydrostatic equilibrium.

The retrieval parameter was projected from the linear scale to the log scale ( $\mathbf{x} \rightarrow \mathbf{z}$ ):

$$\mathbf{z} = \ln(\mathbf{x}). \quad (4)$$

The weighting function  $\mathbf{K}_x$  in the linear scale was also projected onto the log scale,

$$\mathbf{K}_z = \frac{d\mathbf{y}}{dz} = \frac{d\mathbf{y}}{dx} \frac{dx}{dz} = \mathbf{K}_x \mathbf{x}, \quad (5)$$

as well as a variation in the a priori VMR ( $\epsilon_x$ ),

$$\epsilon_z = \ln\left(1 + \frac{\epsilon_x}{\mathbf{x}_a}\right), \quad (6)$$

$$\epsilon_x[i] = \epsilon_1 \mathbf{x}_a[i] + \epsilon_2. \quad (7)$$

The conversion of Eq. (6) is recommended instead of  $\epsilon_z = \epsilon_x / \mathbf{x}_a$  because it avoids quite large values in  $\epsilon_z$  if  $\mathbf{x}_a$  includes a small VMR value (for example on the order of ppt).  $\epsilon_1$  and  $\epsilon_2$  for  $\text{O}_3$  were set to 0.25 and  $1.0 \times 10^{-6}$ , respectively. These values were conservatively estimated from

**Table 2.** Spectroscopic parameters of transitions of  $\text{O}_3$ ,  $^{18}\text{OOO}$  and  $^{17}\text{OOO}$  observed in the spectral windows of TOROROS. The values of intensity and  $\gamma_{\text{air}}$  are assumed at 300 K. Intensity is represented by a base-10 logarithm.  $^{17}\text{OOO}$  has hyperfine structure splittings because of the nuclear spin of  $^{17}\text{O}$ . Only the transition that has the largest line intensity in the series of the hyperfine structure splittings is shown. The updated values from V215 are in bold face.

Species	Window	Frequency [GHz]	Intensity [MHz · nm <sup>2</sup> ]	$\gamma_{\text{air}}$ [MHz Torr <sup>-1</sup> ]	$n_{\text{air}}$ [-]	Quantum numbers		
						$N'_{K'_a, K'_c}$	–	$N''_{K''_a, K''_c}$
$\text{O}_3$	b1	625.3712420 <sup>a</sup>	−3.8748 <sup>b</sup>	<b>3.06<sup>c</sup></b>	<b>0.81<sup>c</sup></b>	15 <sub>6,10</sub>	–	16 <sub>5,11</sub>
$\text{O}_3^*(v2)$	b1/b2	625.6119575 <sup>d</sup>	−6.2140 <sup>d</sup>	2.72 <sup>b</sup>	<b>0.83<sup>b</sup></b>	38 <sub>9,29</sub>	–	39 <sub>8,32</sub>
$^{18}\text{OOO}$	b1/b2	625.5636585 <sup>d</sup>	−3.4532 <sup>b</sup>	2.87 <sup>e</sup>	0.79 <sup>e</sup>	23 <sub>4,19</sub>	–	23 <sub>3,20</sub>
$^{18}\text{OOO}$	c1	<b>649.1371670<sup>d</sup></b>	−3.4919 <sup>b</sup>	2.82 <sup>b</sup>	0.79 <sup>e</sup>	26 <sub>4,23</sub>	–	26 <sub>3,24</sub>
$^{18}\text{OOO}$	c1	<b>649.1386510<sup>d</sup></b>	−4.2063 <sup>b</sup>	2.67 <sup>b</sup>	0.83 <sup>e</sup>	41 <sub>2,39</sub>	–	41 <sub>1,40</sub>
$^{18}\text{OOO}$	c1	<b>649.1515995<sup>d</sup></b>	−4.2237 <sup>b</sup>	2.89 <sup>b</sup>	0.79 <sup>e</sup>	22 <sub>7,16</sub>	–	23 <sub>6,17</sub>
$^{18}\text{OOO}$	c1	<b>649.1524085<sup>d</sup></b>	−4.2237 <sup>b</sup>	2.87 <sup>b</sup>	0.68 <sup>b</sup>	22 <sub>7,15</sub>	–	23 <sub>6,18</sub>
$^{17}\text{OOO}$	c1	649.2752349 <sup>d</sup>	−4.0646 <sup>d</sup>	3.03 <sup>e</sup>	0.77 <sup>e</sup>	14 <sub>4,10</sub>	–	14 <sub>3,11</sub>

<sup>a</sup> Personal communication, H. Ozeki. <sup>b</sup> Personal communication, MLS team (2013). <sup>c</sup> Complex Robert–Bonamy (CRB) calculation performed by Drouin and Gamache (2008). <sup>d</sup> The JPL catalog (Pickett et al., 1998). <sup>e</sup> The HITRAN 2008 database (Rothman et al., 2009).

variations in  $\text{O}_3$  VMR (e.g., Kasai et al., 2013). The variation in  $^{18}\text{OOO}$  in the log scale ( $^{18}\epsilon_z$ ) was given by

$$^{18}\epsilon_z[i] = \sqrt{(^{16}\epsilon_z[i])^2 + (R\epsilon_z[i])^2}. \quad (8)$$

The variation of the isotopic ratio  $R\epsilon_z$  was taken from variations in  $\delta^{18}\text{OOO}$ , and  $R\epsilon_z$  was set to 0.2 for all altitudes. The variations of  $\text{O}_3$  and  $^{18}\text{OOO}$  were multiplied by 2 above 55 km, taking into account an accuracy of the GEOS-5 data.

We implemented cross terms in  $\mathbf{S}_x$  between the ozone isotopomers and isotopologues (such as  $\text{O}_3$  and  $^{18}\text{OOO}$ ) following the retrieval of HDO/ $\text{H}_2\text{O}$  ratios from the Tropospheric Emission Spectrometer (TES) observation (Worden et al., 2006). The retrieval with the cross terms is expected to prevent estimated isotopic ratio from being an unrealistic value and reduce its variations due to measurement errors.

In the cases of retrieval of VMRs of  $\text{O}_3$  and  $^{18}\text{OOO}$  in windows b1 and b2, the covariance matrix for the variations in their a priori profiles was given by

$$\mathbf{S}_z = \begin{pmatrix} ^{16,16}\mathbf{S}_z & ^{16,18}\mathbf{S}_z \\ ^{16,18}\mathbf{S}_z & ^{18,18}\mathbf{S}_z \end{pmatrix}. \quad (9)$$

$^{16,16}\mathbf{S}_z$  and  $^{18,18}\mathbf{S}_z$  are the covariance matrices for  $\text{O}_3$  ( $^{16}z$ ) and  $^{18}\text{OOO}$  ( $^{18}z$ ) in the log scale, respectively. Here we assumed that  $\text{O}_3$  VMRs were uncorrelated with oxygen isotopic ratios (see Appendix A1 for further details).

$$^{mm}\mathbf{S}_z[i, j] = {}^m\epsilon_z[i] {}^m\epsilon_z[j] \exp\left[-\frac{|h[i] - h[j]|}{h_c}\right], \quad (10)$$

where  $m$  is either 16 or 18 and  $i$  and  $j$  in square brackets indicate the index of a matrix or a vector.  $h$  is the vector of the altitude. The correlation length  $h_c$  was set to 6 km.

In the retrieval of window c1,  $^{18}\text{OOO}$  VMR is retrieved with  $^{17}\text{OOO}$ . The cross terms between the two were implemented in the same way as the retrieval of window b1 and b2, but a variation in  $\delta^{17}\text{OOO}$  was assumed to be 0.3.

The retrieval state vector  $z$  was normalized with  $z_a (= \ln(x_a))$  and  $\epsilon_z$  in the retrieval iteration process:

$$\eta = \frac{z - z_a}{\epsilon_z}. \quad (11)$$

The normalized covariance matrix ( $\mathbf{S}_\eta$ ) was given by

$$\mathbf{S}_\eta = \begin{pmatrix} \mathbf{E} & (^{18}\epsilon_z)^{-1} (^{16}\epsilon_z)\mathbf{E} \\ (^{18}\epsilon_z)^{-1} (^{16}\epsilon_z)\mathbf{E} & \mathbf{E} \end{pmatrix}, \quad (12)$$

$$\mathbf{E}[i, j] = \exp\left[-\frac{|h[i] - h[j]|}{h_c}\right]. \quad (13)$$

The solution that minimizes  $\chi^2$  was determined by a Gauss–Newton iterative procedure modified by implementing the Levenberg–Marquardt scheme (Marquardt, 1963):

$$\eta_{r+1} = \eta_r + \left(\mathbf{K}_{\eta_r}^T \mathbf{S}_y^{-1} \mathbf{K}_{\eta_r} + \mathbf{S}_\eta^{-1} + \Gamma \mathbf{U}\right)^{-1} \times \left(\mathbf{K}_{\eta_r}^T \mathbf{S}_y^{-1} (y - \mathbf{F}(x_r)) - \mathbf{S}_\eta^{-1} \eta_r\right); \quad (14)$$

here  $r$  indicates the number of iterations and  $\mathbf{K}_{\eta_r}$  is the weighting function at  $r$ th state  $\eta_r$ :

$$\mathbf{K}_\eta = \frac{\partial y}{\partial \eta} = \frac{\partial y}{\partial z} \frac{\partial z}{\partial \eta} = \mathbf{K}_z \epsilon_z. \quad (15)$$

The Levenberg–Marquardt parameter  $\Gamma$  was increased or decreased during the retrieval iteration by being multiplied by 2 or 1/2 and 5 or 1/5 for band B (windows b0, b1 and b2) and band C (window c1), respectively.  $\mathbf{U}$  is the unit matrix.

**Table 3.** Sources of systematic error and their uncertainties considered in the error analysis. Spectral windows used for the VMR retrieval are shown in parentheses.

Error Sources	Uncertainty			Calculation Equation
	O <sub>3</sub> (b1)	<sup>18</sup> OOO (b2)	<sup>18</sup> OOO (c1)	
$\gamma_{\text{air}}^{\text{a}}$	3 %	6 %	6 %	Eq. (17)
$n_{\text{air}}^{\text{a}}$	10 %	20 %	20 %	Eq. (17)
Line intensity <sup>a</sup>	1 %	2 %	2 %	Eq. (17)
Antenna beam pattern		2 % in FWHM of $R_{\text{ANT}}$		Eq. (17)
SBS characteristics		$\pm 3$ dB in $\beta_{\text{image}}$		Eq. (17)
AOS response function		5 % in FWHM		Eq. (17)
Other source	None	From O <sub>3</sub> line <sup>b</sup>	None	Eq. (17)

<sup>a</sup> Of each observed transition. <sup>b</sup> Uncertainties in the spectroscopic parameters of the O<sub>3</sub> line at 625.371 GHz.

**Table 4.** Same as Table 3 but for random error.

Error Sources	Uncertainty			Calculation Equation
	O <sub>3</sub> (b1)	<sup>18</sup> OOO (b2)	<sup>18</sup> OOO (c1)	
Spectrum noise		0.5 K		Eq. (18)
Smoothing error	Same setting as the retrieval processing for each window			Eq. (20)
Temperature profile	3 K (TR), 10 K (ST), 30 K (ME), and 50 K (TH)*			Eq. (17)
Pressure profile		3 %		Eq. (17)

\* TR: troposphere (0–17 km). ST: stratosphere (17–45 km). ME: mesosphere (45–94 km). TH: thermosphere (94–120 km).

### 3 Performance of SMILES $\delta^{18}\text{OOO}$ observation

We evaluated the  $\delta^{18}\text{OOO}$  retrieved by TOROROS by means of (1) an error analysis and (2) a comparison study.

#### 3.1 Error analysis

We estimated errors in  $\delta^{18}\text{OOO}$  ( $\Delta\delta^{18}\text{OOO}$ ) using

$$\Delta\delta^{18}\text{OOO} = \sqrt{\sum_{m=16,18} \left[ \frac{\partial\delta^{18}\text{OOO}}{\partial^m x} \cdot \Delta^m x \right]^2}, \quad (16)$$

where  $^m x$  and  $\Delta^m x$  denote the VMR value and the error of O<sub>3</sub> ( $m = 16$ ) or <sup>18</sup>OOO ( $m = 18$ ), respectively. The errors  $\Delta^{16}x$  and  $\Delta^{18}x$  were separately calculated for each error source by error analysis with the same methodology described in Sato et al. (2012). The error sources considered in this study are summarized in Tables 3 and 4 for systematic and random errors, respectively. The total systematic and random errors were calculated using the root-sum square of all errors caused by the considered error sources. The error in the tangent height was not included in this error analysis because its systematic error is corrected by the tangent height bias correction described in Sect. 2.1, and Ochiai et al. (2013) estimated that the precision was about 46 m, which was substantially smaller than the interval of altitude grid (about 4–5 km) in TOROROS.

The systematic error includes errors from the model parameters ( $\Delta\mathbf{x}_{\text{param}}$ ) such as spectroscopic parameters and instrument functions.  $\Delta\mathbf{x}_{\text{param}}$  was given by a perturbation method:

$$\Delta\mathbf{x}_{\text{param}} = \mathcal{I}(\mathbf{y}_{\text{ref}}, \mathbf{b}_0 + \Delta\mathbf{b}) - \mathbf{x}_{\text{ref}} \quad (17)$$

$$\mathbf{x}_{\text{ref}} = \mathcal{I}(\mathbf{y}_{\text{ref}}, \mathbf{b}_0), \quad \mathbf{y}_{\text{ref}} = \mathcal{F}(\mathbf{x}_{\text{true}}, \mathbf{b}_0).$$

$\mathcal{I}$  is the function of the inversion calculation.  $\mathbf{b}_0$  and  $\Delta\mathbf{b}$  are the model parameter vector and its uncertainties, respectively. In the error analysis, the VMR profiles of the climatology based on the UARS/MLS observation were assumed as the true states ( $\mathbf{x}_{\text{true}}$ ) for both O<sub>3</sub> and <sup>18</sup>OOO. Any undesirable effects inherent in the retrieval algorithm itself were omitted by using  $\mathbf{x}_{\text{ref}}$  instead of  $\mathbf{x}_{\text{true}}$  in Eq. (17). The values of  $\Delta\mathbf{b}$  were estimated as follows. Uncertainties in the air-broadening parameter ( $\gamma_{\text{air}}$ ) and its temperature dependency ( $n_{\text{air}}$ ) for the O<sub>3</sub> line were estimated to be 3 % and 10 %, respectively, which were typical of errors in past estimations, and that in the line intensity was 1 % (Pickett et al., 1998). For the <sup>18</sup>OOO transition, its spectroscopic parameters' uncertainties were conservatively estimated as being twice the size of those for the O<sub>3</sub> line, considering difficulties in the estimation of the spectroscopic parameters of the isotopomers and isotopologues. Uncertainty in  $R_{\text{ANT}}$  and  $\beta_{\text{image}}$  was 2 % in FWHM and  $\pm 3$  dB, respectively, which are same as the error analysis for the V215 ClO by Sato et al. (2012). Uncertainty in the AOS response function was set to 5 % (Mizobuchi et al., 2012).

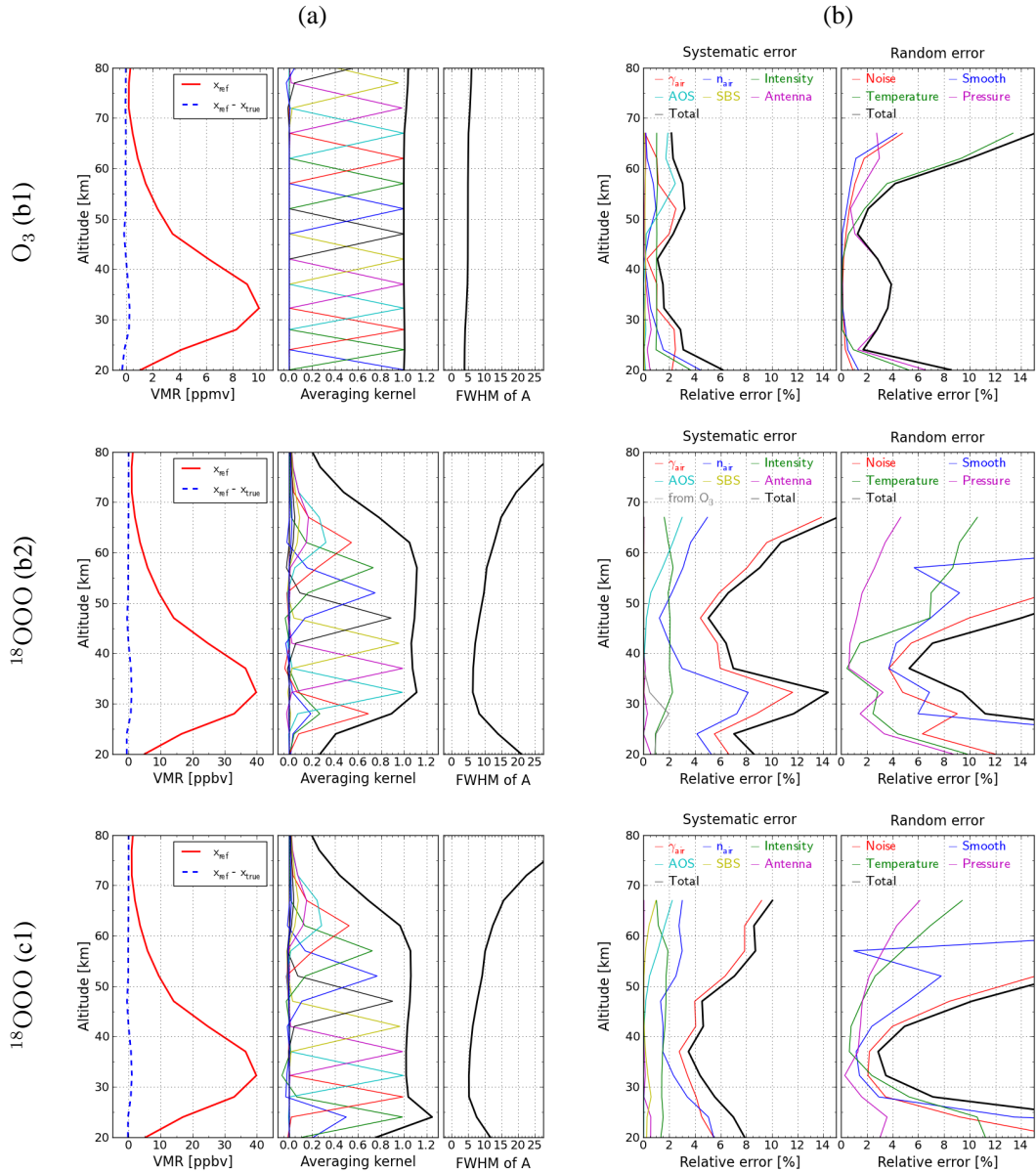


**Fig. 2.** Reference VMR profiles for the error analysis and the relative errors of  $\text{O}_3$  in window b1 (top),  $^{18}\text{O}\text{O}_3$  in window b2 (middle) and  $^{18}\text{O}_3\text{O}$  in window c1 (bottom) retrieved by TOROROS. Column (a) shows the reference profile  $x_{\text{ref}}$  (red) and the difference between  $x_{\text{ref}}$  and the true profile  $x_{\text{true}}$  assumed in the error analysis (blue) in the left panel. The measurement response is represented by the black line, and the averaging kernel for each altitude is displayed in the middle panel. The full width at half maximum (FWHM) of the rows of the averaging kernel matrix is shown in the right panel. Column (b) shows relative errors for the systematic and random errors in the left and right panels, respectively. The random error is for a single-scan observation. The error sources and the estimated uncertainties are listed in Tables 3 and 4.

In this error analysis, the total random error includes an error due to spectrum statistical noise ( $\Delta x_{\text{noise}}$ ), a smoothing error ( $\Delta x_{\text{smooth}}$ ) and errors due to uncertainties in the atmospheric temperature and pressure profiles.  $\Delta x_{\text{noise}}$  was calculated using

$$\Delta x_{\text{noise}}[i] = \sqrt{\mathbf{S}_{\text{noise}}[i, i]}, \quad (18)$$

$$\mathbf{S}_{\text{noise}} = \mathbf{D}\mathbf{S}_y\mathbf{D}^T,$$

where  $i$  in a square bracket indicates an index of a matrix or a vector.  $\mathbf{S}_{\text{noise}}$  is the covariance matrix for spectrum noise.  $\mathbf{D}$  is the contribution function matrix and is given by

$$\mathbf{D} = \frac{\partial \hat{\mathbf{x}}}{\partial \mathbf{y}} = \left( \mathbf{K}_x^T \mathbf{S}_y^{-1} \mathbf{K}_x + \mathbf{S}_x^{-1} \right)^{-1} \mathbf{K}_x^T \mathbf{S}_y^{-1}, \quad (19)$$

where  $\hat{\mathbf{x}}$  is a retrieval solution of  $\mathbf{x}$ .  $\Delta\mathbf{x}_{\text{smooth}}$  was calculated using

$$\Delta\mathbf{x}_{\text{smooth}}[i] = \sqrt{\mathbf{S}_{\text{smooth}}[i, i]} \quad (20)$$

$$\mathbf{S}_{\text{smooth}} = (\mathbf{A} - \mathbf{U})\mathbf{S}_z(\mathbf{A} - \mathbf{U})^T.$$

Here,  $\mathbf{S}_{\text{smooth}}$  is the covariance matrix for errors derived from  $\mathbf{S}_z$  given by Eq. (10) and  $\mathbf{A}$  is the averaging kernel matrix.

$$\mathbf{A} = \frac{\partial \hat{\mathbf{x}}}{\partial \mathbf{x}} = \mathbf{D}\mathbf{K}. \quad (21)$$

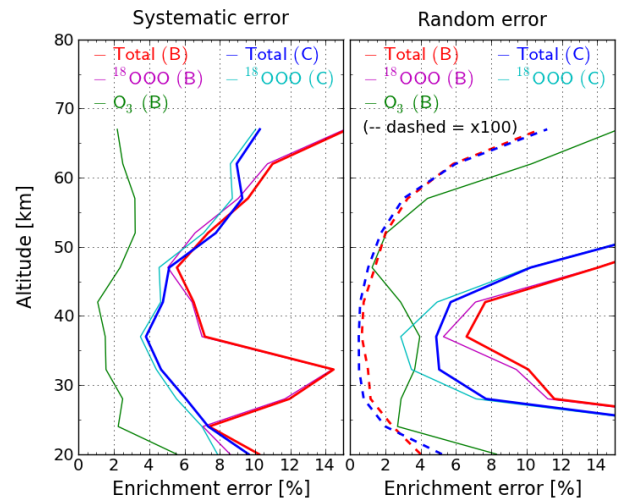
The errors due to uncertainties in the atmospheric temperature and pressure profiles were calculated via Eq. (17) taking into account a vertical correlation between different altitudes (see Eqs. 25–30 in Sato et al., 2012).

Figure 2 shows the reference VMR profiles ( $\mathbf{x}_{\text{ref}}$ ) and the averaging kernels in the left column. The results of the error analysis for the VMRs of  $\text{O}_3$  in window b1 and  $^{18}\text{O}$  in windows b2 and c1 are shown in the right column. The differences between  $\mathbf{x}_{\text{ref}}$  and  $\mathbf{x}_{\text{true}}$  for all molecules were almost zero, implying that the errors inherent in the algorithm itself were negligibly small. The same retrieval grid was employed for all retrieval windows in order to obtain the isotopic ratio without recourse to any vertical interpolation in TOROROS, while V215 adjusted the retrieval grid to optimize each molecule (see Fig. A1). The error analysis for the V215 product is described in Appendix A2. The measurement response  $\mathbf{m}$  is given by

$$\mathbf{m}[i] = \sum_j |\mathbf{A}[i, j]|, \quad (22)$$

and indicates a sensitivity of the observation to the retrieved result (see Eq. 19 in Sato et al., 2012, and references therein); that is, values of  $\mathbf{m}$  near unity indicate that most information in the retrieval results is provided by observations, while low values of  $\mathbf{m}$  indicate that the retrieval results are largely influenced by the a priori state and forced to be identical to the a priori values. The  $\mathbf{m}$  values of b1  $\text{O}_3$  were almost equal to unity for all altitudes between 20 and 80 km. For  $^{18}\text{O}$  in the windows b2 and c1, the  $\mathbf{m}$  values were larger than 0.9 at altitudes between 28 and 62 km. The FWHM of rows of  $\mathbf{A}$  for the b1  $\text{O}_3$  VMR was about 5 km at altitudes from 20 to 80 km, and those for  $^{18}\text{O}$ s were increased from 5 to 10 km at altitude levels of 28–57 km.

The total systematic error of the b1  $\text{O}_3$  was about 2–3 % from 25 to 65 km. Large contributions were from  $\gamma_{\text{air}}$ , the line intensity and the AOS response function. Below 55 km,  $\gamma_{\text{air}}$  and the line intensity were the dominant causes of the error. The AOS became more important above 50 km. Compared with the errors of the V215  $\text{O}_3$  (see Fig. A1), the errors of the  $\text{O}_3$  VMR in TOROROS were considerably decreased, which was not the case for the retrievals of  $^{18}\text{O}$ . This improvement is derived from the retrievals of  $\text{O}_3$  and  $^{18}\text{O}$  using the same tangent height. In the TOROROS algorithm,



**Fig. 3.** Errors in the enrichment  $\delta^{18}\text{O}$  obtained by TOROROS. Systematic and random errors are shown in the left and right panels, respectively. Random errors are represented by solid and dashed lines for a single-scan observation and the average of 100 profiles, respectively. Total errors in  $\delta^{18}\text{O}$  from the  $^{18}\text{O}$ s in windows b2 and c1 are represented by red and blue lines. The purple, light-blue and green lines show the errors in  $\delta^{18}\text{O}$  caused by the error sources in the retrievals of  $^{18}\text{O}$  (window b2),  $^{18}\text{O}$  (window c1) and  $\text{O}_3$  (window b1), respectively.

the tangent height was fixed and the error propagation of  $\gamma_{\text{air}}$  was minimized. If the tangent height was retrieved, it was largely dependent on  $\gamma_{\text{air}}$ , and this contribution was increased as in V215. The improvement of the AOS response function was also important for reducing the error. The total random error for a single-scan observation was 2–4 % between 25 and 55 km. Errors from the atmospheric pressure profile were the largest below 45 km and those from the temperature profile were the largest above 50 km.  $\Delta\mathbf{x}_{\text{noise}}$  and  $\Delta\mathbf{x}_{\text{smooth}}$  were less than 1 % between 25 and 50 km because of high S/N ratios of the  $\text{O}_3$  transition.

The total systematic error in the  $^{18}\text{O}$  VMR retrieved in window b2 varied from 5 to 15 %. It took a minimum value at altitudes between 40 and 50 km, and increased below and above this altitude region. The largest contribution was made by the uncertainty in  $\gamma_{\text{air}}$ . Similar to  $\text{O}_3$ , errors from the AOS response function were decreased compared to V215 (see Fig. A1). The total random error was larger than 5 % and increased to 20 % above 40 km. Errors due to the spectrum noise and smoothing error were more dominant than the errors from the atmospheric temperature and pressure profiles, which is the opposite of the random error of  $\text{O}_3$ . The smoothing error seems to be oscillated, which is due to the use of cross terms in  $\mathbf{S}_x$ . Both systematic and random errors in the c1  $^{18}\text{O}$  were almost the same as the b2  $^{18}\text{O}$ , except for errors from  $\gamma_{\text{air}}$  around 32 km and from temperature profiles above 45 km.

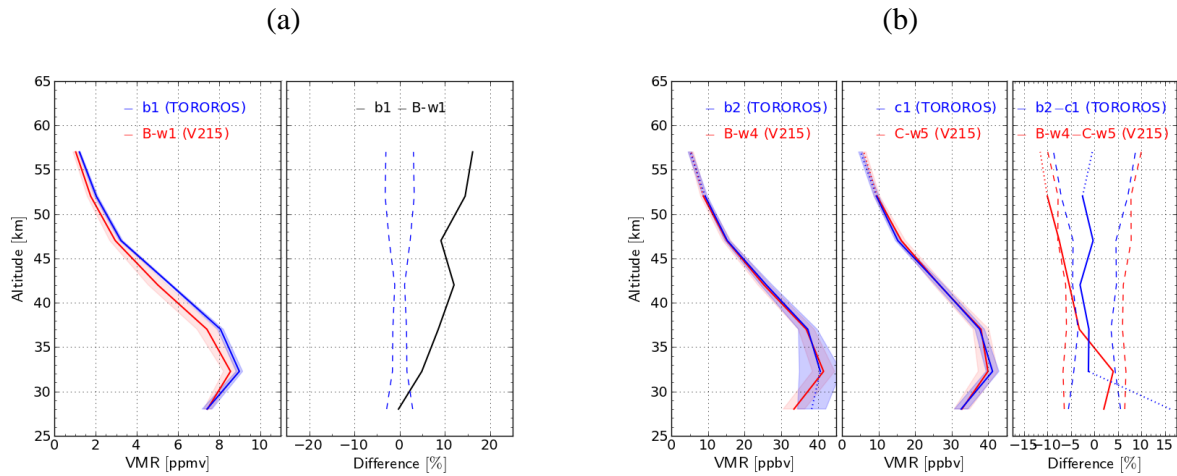


**Fig. 4.** Comparison between VMRs of  $\text{O}_3$  (a) and  $^{18}\text{O}\text{O}_3$  (b) retrieved by TOROROS (blue) and V215 (red). Latitude:  $20\text{--}40^\circ\text{N}$ . Month: February–March (2010). Solar zenith angle:  $< 80^\circ$  (daytime). Only data with “good quality” (see text) are used for this comparison. The systematic errors estimated by the error analysis are represented by the shaded area. In column (a), the left panel shows the median value of TOROROS and V215. The right panel does their difference and systematic error in TOROROS by solid and dashed lines, respectively. Column (b) shows the same as column (a) but for  $^{18}\text{O}\text{O}_3$  VMRs in bands B and C. The dotted line represents data for which the deviation is large or the number of profiles is small. The dashed lines are for the systematic errors in band C.

We estimated the errors of the isotopic enrichment by means of Eq. (16) using the errors of  $\text{O}_3$  in window b1 and  $^{18}\text{O}\text{O}_3$  in windows b2 and c1. The systematic and random errors of  $\delta^{18}\text{O}\text{O}_3$  were calculated in the same manner, and the results are shown in Fig. 3. The systematic errors for the b2 and c1  $^{18}\text{O}\text{O}_3$ s showed similar values of 6% at 45 km and increased to more than 10% at altitudes higher than 60 km. However, the errors in  $\delta^{18}\text{O}\text{O}_3$  from the b2  $^{18}\text{O}\text{O}_3$  were larger than those from the c1  $^{18}\text{O}\text{O}_3$  of 4–6% at altitudes between 25 and 40 km. This is because of the large error due to the uncertainty in  $\gamma_{\text{air}}$  of the  $^{18}\text{O}\text{O}_3$  transition in window b2. Errors from  $^{18}\text{O}\text{O}_3$  were dominant, rather than  $\text{O}_3$ , for both  $\delta^{18}\text{O}\text{O}_3$ s calculated using windows b2 and c1. The error contributed from  $\text{O}_3$  was about 2–4% and was decreased compared with that of V215 (see Fig. A2). The random error from the c1  $^{18}\text{O}\text{O}_3$  was smaller than that from the b2  $^{18}\text{O}\text{O}_3$  for a single-scan observation. It took the minimum values of 5% between 30 and 40 km, where the VMRs of  $\text{O}_3$  and  $^{18}\text{O}\text{O}_3$  were the maximums, and was increased to more than 15% below and above this altitude region. Similar to the systematic error, the contribution of errors from  $^{18}\text{O}\text{O}_3$  was larger than that from  $\text{O}_3$ . In general, random errors are suppressed by averaging the number of profiles. Given these characteristics, the random error was decreased to less than 2% at altitudes from 25 to 50 km by averaging 100 profiles, which was the case for both windows b2 and c1.

In conclusion regarding the error analysis, the largest error source in  $\delta^{18}\text{O}\text{O}_3$  was the  $\gamma_{\text{air}}$  of the  $^{18}\text{O}\text{O}_3$  transition. Indeed, this error source contributed more than 90% to the total systematic error. It is worth noting that the accuracy of spectroscopic parameters, especially  $\gamma_{\text{air}}$ , is essential for

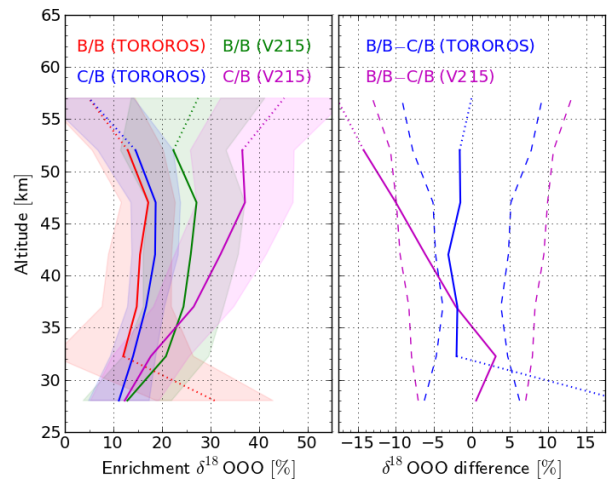


**Fig. 5.** Comparison of  $\delta^{18}\text{O}\text{O}_3$  between TOROROS and V215 in bands B and C. The ranges of latitude, month and SZA were the same as the comparison in Fig. 4. Only data with “good quality” were used in this study. The red and blue lines represent the  $\delta^{18}\text{O}\text{O}_3$  calculated by the  $^{18}\text{O}\text{O}_3$  of band B (window b2) and band C (window c1), respectively. The  $\text{O}_3$  of band B (window b1) is common to both  $^{18}\text{O}\text{O}_3$ s. The green and purple lines are  $\delta^{18}\text{O}\text{O}_3$  for the product of V215. The shaded areas represent the systematic errors estimated by the error analyses (see Figs. 3 and A2). The differences between bands B and C are shown in the right panel by the blue and purple lines for TOROROS and V215, respectively. The dotted line represents data for which the deviation is large or the number of profiles is small. The dashed lines show the systematic errors in  $\delta^{18}\text{O}\text{O}_3$  from band C  $^{18}\text{O}\text{O}_3$ .

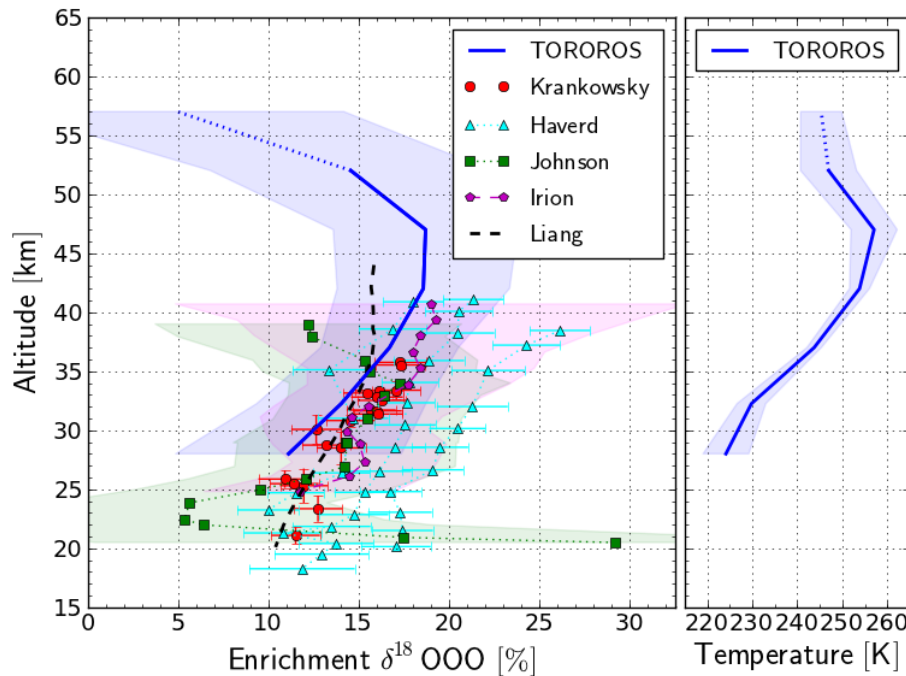


**Fig. 6.** Comparison of  $\delta^{18}\text{OOO}$  derived from the SMILES observation by TOROROS with the past measurements. The blue line represents the TOROROS  $\delta^{18}\text{OOO}$  obtained from the b1  $\text{O}_3$  and the c1  $^{18}\text{OOO}$ . The data selection is the same as the other comparisons in this paper (Figs. 4–5). The estimated systematic error for each case is represented by the respective shaded area. See the caption of Fig. 4 for an explanation of the dotted line. The red circle denotes the observations using a mass spectrometer (Krankowsky et al., 2007). The error bar represents the 1- $\sigma$  standard deviation. These data are multiplied by a factor of 1.196 (= 12.2/10.2) to translate from  $\delta^{18}\text{O}$  (bulk) to  $\delta^{18}\text{OOO}$ . The factor is estimated from the observation by Johnson et al. (2000), whose measurement results are shown as solid green squares for the estimated precisions. The light-blue triangle represents the observations of Haverd et al. (2005). The error bar represents the estimated precision. The ATMOS observation (Irion et al., 1996) is represented by purple marker with shaded area of the 1- $\sigma$  standard deviation. The black dashed line is the 1-D model simulation of  $\delta^{18}\text{OOO}$  by Liang et al. (2006). Further information on the past measurements is shown in Table 5. Note that the error bars and the shaded areas are used to distinguish between errors in one measurement and in averaged values of several measurements, respectively. The vertical temperature profile retrieved from the SMILES observation is shown (window b0) in the right panel. Shaded area represents the estimated systematic error in the temperature.

reducing errors in remote-sensing measurements with a high S/N ratio spectrum (Sato et al., 2012; Sagawa et al., 2013; Kasai et al., 2013). We recommend that a laboratory study be undertaken to determine  $\gamma_{\text{air}}$  of  $^{18}\text{OOO}$  transitions at an accuracy on at least the same order of that of the  $\text{O}_3$  transition (3 %), although both laboratory experiments and theoretical predictions have large difficulties that must be overcome.

### 3.2 Comparison

We compared the VMRs of  $\text{O}_3$  and  $^{18}\text{OOO}$  derived from SMILES observation by TOROROS and V215. This comparison was performed using a profile-by-profile comparison. We selected the VMR profiles derived from the same scan by TOROROS and V215 under the following conditions: 20–40° N, February–March (2010) and  $\text{SZA} < 80^\circ$ . The daytime condition was chosen since most of the past measurements compared with TOROROS later (see Fig. 6) have been during daytime. The comparison results for nighttime are shown in Appendix A3.

In this study we selected data that are regarded as “good quality” by  $\chi^2$  and measurement response  $m$ . About 20 % of the data with larger  $\chi^2$  values were removed, and only the retrieved data at altitude levels that satisfy  $0.9 < m < 1.2$  were used. The L1b data with field-of-view interferences were also removed. The numbers of  $\delta^{18}\text{OOO}$  profiles calculated from the b1  $\text{O}_3$  and the c1  $^{18}\text{OOO}$  with “good quality” were 1145–1377 in an altitude range between 28 and 57 km.

The left panel of Fig. 4 shows the comparison of the  $\text{O}_3$  VMRs retrieved by TOROROS (window b1) and by V215 (window B-w1; see Table A1) between 28 and 57 km. The median statistic was used instead of the mean statistic for average state. The B-w1  $\text{O}_3$  VMR was linearly interpolated on the retrieval grid of the b1  $\text{O}_3$ . The b1  $\text{O}_3$  VMR was larger than the B-w1  $\text{O}_3$  VMR by at most 0.6 ppmv at altitudes above 32 km. This is plausible, since Kasai et al. (2013) showed that the B-w1  $\text{O}_3$  VMR had a negative bias in this altitude region (−0.5 to −1.0 ppmv) due to a problem of tangent height determination caused by uncertainty in the non-linearity gain calibration of spectrum brightness temperature.

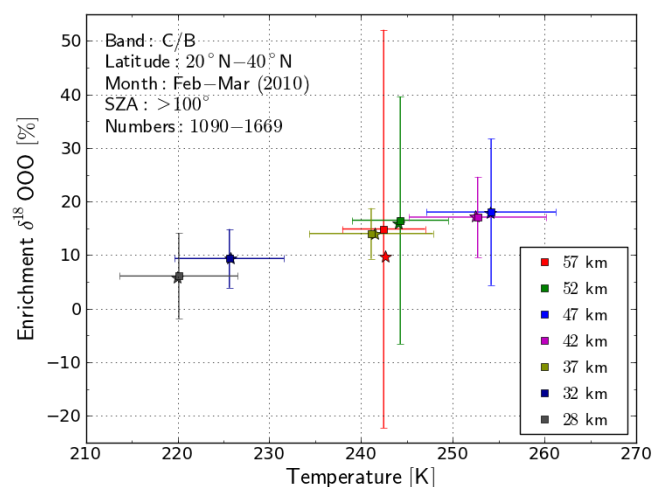


**Fig. 7.** Correlation between  $\delta^{18}\text{O}^{\text{OO}}$  and temperature derived from the SMILES observation.  $\delta^{18}\text{O}^{\text{OO}}$  is calculated using the b1  $\text{O}_3$  and c1  $^{18}\text{O}^{\text{OO}}$ . The temperature was retrieved in window b0 of TOROROS. Latitude:  $20^\circ\text{N}$ – $40^\circ\text{N}$ . Month: February–March (2010). Solar zenith angle:  $>100^\circ$  (nighttime). Only data with “good quality” (see text) were used. The number of the average for each altitude is shown (the minimum and the maximum values). The mean value for each altitude is plotted as a square marker with an error bar of  $1\text{-}\sigma$  standard deviation. The median value is plotted as a star marker.

The comparison for  $^{18}\text{O}^{\text{OO}}$  VMR is shown in the right side of Fig. 4. The B-w4 and C-w5 windows of V215 correspond to the b2 and c1 of TOROROS, respectively. The  $^{18}\text{O}^{\text{OO}}$  VMRs derived by TOROROS and V215 are in good agreement within the systematic errors for both bands B and C. Only b2  $^{18}\text{O}^{\text{OO}}$  showed larger VMR than the others at 28 km (represented by dotted line). The difference of  $^{18}\text{O}^{\text{OO}}$  VMR between bands B and C in the TOROROS algorithm was less than 1 ppbv at altitudes between 32 and 57 km. The use of common tangent height values in the processing of those two bands largely contributed to the reduction of the bias between bands B and C. In V215, the tangent height values were optimized for each band processing, which resulted in the significant  $^{18}\text{O}^{\text{OO}}$  difference between bands B and C.

Figure 5 shows the comparison of  $\delta^{18}\text{O}^{\text{OO}}$  between TOROROS and V215. The  $\delta^{18}\text{O}^{\text{OO}}$ s of TOROROS were 10–20 % between 32 and 57 km and were smaller than those of V215. This is because of larger values of the b1  $\text{O}_3$  VMR (in TOROROS) than those of the B-w1  $\text{O}_3$  (in V215), as shown in Fig. 4. The b2  $^{18}\text{O}^{\text{OO}}$  VMR at 28 km made  $\delta^{18}\text{O}^{\text{OO}}$  larger than 30 %. We recommend that data at this altitude not be used. At 57 km, a dispersion of  $\delta^{18}\text{O}^{\text{OO}}$  was quite large and we recommend the use of the  $\delta^{18}\text{O}^{\text{OO}}$  value only for a qualitative discussion, not for a quantitative one. The discrepancies of TOROROS  $\delta^{18}\text{O}^{\text{OO}}$  between bands B and C were less than 3 %, which was smaller than those of

V215, at altitude levels between 32 and 57 km. A decrease of  $\delta^{18}\text{O}^{\text{OO}}$  was observed in both TOROROS and V215 between 47 and 52 km, which is discussed in Sect. 4.

The TOROROS  $\delta^{18}\text{O}^{\text{OO}}$  was compared with previous  $\delta^{18}\text{O}^{\text{OO}}$  measurements in Fig. 6. The  $\delta^{18}\text{O}^{\text{OO}}$  from the b1  $\text{O}_3$  and the c1  $^{18}\text{O}^{\text{OO}}$  is shown by the blue line. The TOROROS  $\delta^{18}\text{O}^{\text{OO}}$  increased from 13 to 18 % as the altitude increased from 32 to 42 km. This is in good agreement with other measurements within the systematic errors of TOROROS  $\delta^{18}\text{O}^{\text{OO}}$  in this altitude range. The gradient of the TOROROS  $\delta^{18}\text{O}^{\text{OO}}$  was about  $+0.5\%$   $\text{km}^{-1}$ , which was also consistent with the ATMOS observation (Irion et al., 1996). Temperature retrieved by TOROROS, in window b0, is also shown in Fig. 6, and the TOROROS  $\delta^{18}\text{O}^{\text{OO}}$  seems to be correlated with the temperature. The correlation between  $\delta^{18}\text{O}^{\text{OO}}$  and temperature is discussed in Sect. 4.

### 3.3 Summary of the error of the SMILES $\delta^{18}\text{O}^{\text{OO}}$

The systematic and random errors in the  $\delta^{18}\text{O}^{\text{OO}}$  derived by TOROROS are summarized in Table 6. The total systematic error estimated by the error analysis was about 5–15 % at altitudes between 32 and 57 km (see Fig. 3). The dominant source of error was the uncertainty in  $\gamma_{\text{air}}$  of the  $^{18}\text{O}^{\text{OO}}$  transition for both windows b2 and c1. The total random error was less than 2 % by averaging 100 profiles in this altitude region. The comparison studies showed that the TOROROS  $\delta^{18}\text{O}^{\text{OO}}$  was in good agreement with the past measurements within the estimated systematic error in the altitude range between 30 and 40 km (see Fig. 6).

## 4 Discussion

Here we discuss in detail the  $\delta^{18}\text{O}^{\text{OO}}$  decrease derived by TOROROS with increasing altitude above 45 km. As reported by Morton et al. (1990) and Krankowsky et al. (2007), oxygen isotopic fractionation in the ozone formation (Reaction R1) has a significant temperature dependence. Figure 7 shows the correlation between  $\delta^{18}\text{O}^{\text{OO}}$ , calculated from b1  $\text{O}_3$  and c1  $^{18}\text{O}^{\text{OO}}$ , as well as temperature from b0 derived by TOROROS. In order to minimize photolysis effects, only nighttime data ( $\text{SZA} > 100^\circ$ ) were plotted. The mean and median  $\delta^{18}\text{O}^{\text{OO}}$  values agreed within 1 % except at 57 km, and they can be regarded as representative values between 28 and 52 km. There is a clear positive correlation between  $\delta^{18}\text{O}^{\text{OO}}$  and temperature, strongly suggesting that the ozone isotopic enrichment increases with temperature. This behavior is qualitatively consistent with experiments reported by Morton et al. (1990) and Krankowsky et al. (2007), although their experiments were for the bulk  $\delta^{50}\text{O}_3$ . The gradient of the TOROROS  $\delta^{18}\text{O}^{\text{OO}}$  against temperature was roughly estimated to be about  $0.25\%$   $\text{K}^{-1}$ . The chaperon mechanism (i.e.,  $\text{ArO} + \text{O}_2 \rightarrow \text{Ar} + \text{O}_3$  and  $\text{ArO}_2 + \text{O} \rightarrow \text{Ar} + \text{O}_3$ ) should also be considered as an alternative to explain

**Table 5.** Summary of information from SMILES and past measurements used in the comparison shown in Fig. 5.

Instrument	Latitude*	Month/year*	Altitude	Reference
SMILES (from ISS)	20–40° N	Feb–Mar 2010	32–57 km	This paper
Mass spectrometry of collected ozone by balloon	43.7° N	3 Oct 1998, 11 Oct 1999, 4 Oct 2000 11 May 2001, 25 Apr 2002	21–36 km	Krankowsky et al. (2007)
JPL MkIV FTIR spectrometer (balloon-based)	34° N	9 Mar 1993, 14 Feb 1994, 27 Feb 1996	18–41 km	Haverd et al. (2005)
FIRS-2 FT spectrometer (balloon-based)	30–35° N, 68° N (in 1997)	26 Sep 1989, 4 Jun 1990, 29 May 1992, 29 Sep 1992, 23 Mar 1993, 22 May 1994 30 Apr 1997	20–40 km	Johnson et al. (2000)
ATMOS FTIR spectrometer (space-based)	80° S–80° N	Apr 1985, Apr 1992 May 1993, Nov 1994	25–41 km	Irion et al. (1996)

\* Note that the information is only for this comparison and not for all observations.

**Table 6.** Summary of the error in  $\delta^{18}\text{O}$  derived from the SMILES observation by TOROROS. The numbers on the left and right side are for  $\delta^{18}\text{O}$  from the b2  $^{18}\text{O}$  and the c1  $^{18}\text{O}$ , respectively, for the median value of  $\delta^{18}\text{O}$ , SE, RE (1) and RE (100).

Altitude	$\delta^{18}\text{O}$ <sup>a</sup>	SE <sup>b</sup>	RE (1) <sup>c</sup>	RE (100) <sup>d</sup>	FWHM of A <sup>e</sup>	Main error source
52 km	15 %/18 %	8 %/7 %	20 %/17 %	2 %/2 %	9 km	$\gamma_{\text{air}}$ of the $^{18}\text{O}$ transition
42 km	16 %/20 %	7 %/5 %	8 %/6 %	1 %/1 %	6 km	$\gamma_{\text{air}}$ of the $^{18}\text{O}$ transition
32 km	15 %/13 %	14 %/5 %	10 %/5 %	1 %/1 %	5 km	$\gamma_{\text{air}}$ of the $^{18}\text{O}$ transition

<sup>a</sup> Median value under the conditions of 20°N–40°N, February–March (2010) and SZA < 80°. <sup>b</sup> Systematic error. <sup>c</sup> Random error for a single-scan observation. <sup>d</sup> Random error in the average of 100 profiles. <sup>e</sup> Full width at half maximum of the averaging kernel matrix.

the  $\delta^{18}\text{O}$  decrease with increasing altitude (Ivanov and Schinke, 2006). Since the  $\delta^{18}\text{O}$  decrease with increasing altitude was observed during not only daytime but also nighttime (see Fig. A4), the photolysis (Reaction R2) could not be responsible for the  $\delta^{18}\text{O}$  decrease with increasing altitude. Ozone isotopic enrichment is assumed to be less dependent on pressure, particularly lower than 50 hPa (> 20 km) (e.g., Gao and Marcus, 2002). There have been previous experiments on ozone isotopic enrichment as a function of pressure using  $\text{O}_3$  produced by UV photolysis and the discharge of  $\text{O}_2$  (Thiemens and Jackson, 1987; Morton et al., 1990). A certain decrement of the enrichment was measured at pressures lower than 8 hPa; however, the authors mentioned that it might be due to an apparatus effect. Further investigation is suggested in order to clarify a role that pressure plays on the ozone isotopic enrichment, especially for pressures lower than 1 hPa.

We also investigated whether or not the  $\delta^{18}\text{O}$  decrease with increasing altitude is caused by errors in the SMILES observations. The error from  $\gamma_{\text{air}}$  of the  $^{18}\text{O}$  transition, which is the largest error source in the total systematic error of  $\delta^{18}\text{O}$ , is unlikely to explain the  $\delta^{18}\text{O}$  decrease with increasing altitude because, firstly, the  $\delta^{18}\text{O}$  decrease with increasing altitude was observed by two separate observations from frequency bands B and C (see Fig. 5) and, secondly, the TOROROS  $\delta^{18}\text{O}$  (absolute value and gradient) is in good agreement with the other measurements in the stratosphere. This would not be the case if the  $\gamma_{\text{air}}$  value

were not realistic. The systematic error in  $\delta^{18}\text{O}$  due to the errors in b1  $\text{O}_3$  VMR was estimated to be less than 4 % (see Fig. 2), which is smaller than the amplitude of the  $\delta^{18}\text{O}$  decrease with increasing altitude. We also confirmed a priori dependence of  $\delta^{18}\text{O}$  by applying a perturbation of 100 % and obtained almost the same result, with a difference within 1–2 %. Thus, the error of the TOROROS observation considered in this paper cannot explain the  $\delta^{18}\text{O}$  decrease with increasing altitude.

We concluded that temperature could be a dominant factor in controlling of  $\delta^{18}\text{O}$  vertical profile in an altitude range of 28 to 52 km.

## 5 Conclusions

We derived  $\delta^{18}\text{O}$  using a retrieval algorithm, named TOROROS, optimized for oxygen isotopic ratio in ozone in a range between the middle stratosphere and the lower mesosphere from SMILES observations. The TOROROS algorithm is based on the V215 algorithm and includes (i) an a priori covariance matrix constrained by oxygen isotopic ratios in ozone, (ii) an optimization of spectral windows for ozone isotopomers and isotopologues, and (iii) common tangent height information for all windows. The TOROROS  $\delta^{18}\text{O}$  was 13 % at 32 km and the systematic error was estimated to be about 5 %. The systematic and random errors were estimated by a quantitative error analysis. The largest

error source was the uncertainty in  $\gamma_{\text{air}}$  of the  $^{18}\text{O}$  transition, accounting for more than 90 % of the total systematic error. Determination of  $\gamma_{\text{air}}$  of the  $^{18}\text{O}$  transitions with an accuracy better than at least 3 % is desirable for the  $\delta^{18}\text{O}$  using the SMILES observation and for other molecules as well.

The TOROROS  $\delta^{18}\text{O}$  was consistent with those of the past measurements within the estimated systematic errors at altitudes between 30 and 40 km. The vertical profile of  $\delta^{18}\text{O}$  obtained in this work showed an increase and a decrease with increasing altitude in the stratosphere and mesosphere, respectively. The  $\delta^{18}\text{O}$  peak, 18 %, is found at the stratopause. The TOROROS  $\delta^{18}\text{O}$  had a positive correlation with temperature in a range of 220–255 K. Since the  $\delta^{18}\text{O}$  decrease with increasing altitude in the lower mesosphere was observed during both daytime and nighttime, ozone photolysis might not be a dominant factor for this behavior in  $\delta^{18}\text{O}$ .

In this work, we have provided the first observation of  $\delta^{18}\text{O}$  over a range as wide as from the stratosphere to the lower mesosphere. Temperature is likely a dominant factor that controls vertical profile of  $\delta^{18}\text{O}$  in the altitude range of 28 to 52 km.

*Acknowledgements.* The JEM/SMILES mission is a joint project of the Japan Aerospace Exploration Agency (JAXA) and the National Institute of Information and Communications Technology (NICT). Data processing and other research tasks in the present study were performed with the NICT Science Cloud at NICT as a collaborative research project. The authors wish to acknowledge K. Kikuchi, S. Ochiai (NICT), M. Shiotani (Kyoto University), M. Suzuki (ISAS/JAXA) and colleagues at JAXA and NICT for managing and supporting the SMILES mission. The authors are grateful to K. A. Walker (Toronto University) and M. Mahani (Tohoku University) for scientific and technical discussion. T. O. Sato thanks the members of Yoshida Group (Tokyo Institute of Technology). The authors also thank K. Muranaga and T. Haru (Systems Engineering Consultants Co. Ltd.) and J. Möller (Molflow Co. Ltd.) for supporting the data processing of the level-2 research product. T. O. Sato is supported by a grant-in-aid for Research Fellowship for Young Scientists DC1 (No. 23-9766) from the Japan Society for the Promotion of Science, and by the Global COE program “Earth to Earths” of the Ministry of Education, Culture, Sports, and Technology, Japan. Y. Kasai is supported by the Funding Program for Next Generation World-Leading Researchers (NEXT Program) (No. GR101).

Edited by: J. Joiner

## References

- Baron, P., Urban, J., Sagawa, H., Möller, J., Murtagh, D. P., Mendrok, J., Dupuy, E., Sato, T. O., Ochiai, S., Suzuki, K., Manabe, T., Nishibori, T., Kikuchi, K., Sato, R., Takayanagi, M., Murayama, Y., Shiotani, M., and Kasai, Y.: The Level 2 research product algorithms for the Superconducting Submillimeter-Wave Limb-Emission Sounder (SMILES), *Atmos. Meas. Tech.*, 4, 2105–2124, doi:10.5194/amt-4-2105-2011, 2011.
- Drouin, B. J. and Gamache, R. R.: Temperature dependent air-broadened linewidths of ozone rotational transitions, *J. Mol. Spectrosc.*, 251, 194–202, doi:10.1016/j.jms.2008.02.016, 2008.
- Gao, Y. Q. and Marcus, R. A.: Strange and unconventional isotope effects in ozone formation, *Science*, 293, 259–263, doi:10.1126/science.1058528, 2001.
- Gao, Y. Q. and Marcus, R. A.: On the theory of the strange and unconventional isotopic effects in ozone formation, *J. Chem. Phys.*, 116, 137–154, doi:10.1063/1.1415448, 2002.
- Hathorn, B. C. and Marcus, R. A.: An intramolecular theory of the mass-independent isotope effect for ozone. I, *J. Chem. Phys.*, 111, 4087–4100, doi:10.1063/1.480267, 1999.
- Haverd, V., Toon, G. C., and Griffith, D. W. T.: Evidence for altitude-dependent photolysis-induced  $^{18}\text{O}$  isotopic fractionation in stratospheric ozone, *Geophys. Res. Lett.*, 32, L22808, doi:10.1029/2005GL024049, 2005.
- Hedin, A. E.: Extension of the MSIS thermosphere model into the middle and lower atmosphere, *J. Geophys. Res.*, 96, 1159–1172, doi:10.1029/90JA02125, 1991.
- Irion, F. W., Gunson, M. R., Rinsland, C. P., Yung, Y. L., Abrams, M. C., Chang, A. Y., and Goldman, A.: Heavy ozone enrichments from ATMOS infrared solar spectra, *Geophys. Res. Lett.*, 23, 2377–2380, doi:10.1029/96GL01695, 1996.
- Ivanov, M. V. and Schinke, R.: Recombination of ozone via the chaperon mechanism, *J. Chem. Phys.*, 124, 104303, doi:10.1063/1.2174013, 2006.
- Johnson, D. G., Jucks, K. W., Traub, W. A., and Chance, K. V.: Isotopic composition of stratospheric ozone, *J. Geophys. Res.*, 105, 9025–9031, doi:10.1029/1999JD901167, 2000.
- Kasai, Y. J., Urban, J., Takahashi, C., Hoshino, S., Takahashi, K., Inatani, J., Shiotani, M., and Masuko, H.: Stratospheric ozone isotope enrichment studied by submillimeter wave heterodyne radiometry: the observation capabilities of SMILES, *IEEE T. Geosci. Remote*, 44, 676–693, doi:10.1109/TGRS.2005.861754, 2006.
- Kasai, Y., Sagawa, H., Kreyling, D., Dupuy, E., Baron, P., Mendrok, J., Suzuki, K., Sato, T. O., Nishibori, T., Mizobuchi, S., Kikuchi, K., Manabe, T., Ozeki, H., Sugita, T., Fujiwara, M., Irimajiri, Y., Walker, K. A., Bernath, P. F., Boone, C., Stiller, G., von Clarmann, T., Orphal, J., Urban, J., Murtagh, D., Llewellyn, E. J., Degenstein, D., Bourassa, A. E., Lloyd, N. D., Froidevaux, L., Birk, M., Wagner, G., Schreier, F., Xu, J., Vogt, P., Trautmann, T., and Yasui, M.: Validation of stratospheric and mesospheric ozone observed by SMILES from International Space Station, *Atmos. Meas. Tech.*, 6, 2311–2338, doi:10.5194/amt-6-2311-2013, 2013.
- Kikuchi, K., Nishibori, T., Ochiai, S., Ozeki, H., Irimajiri, Y., Kasai, Y., Koike, M., Manabe, T., Mizukoshi, K., Murayama, Y., Nagahama, T., Sano, T., Sato, R., Seta, M., Takahashi, C., Takayanagi, M., Masuko, H., Inatani, J.,

- Suzuki, M., and Shiotani, M.: Overview and early results of the Superconducting Submillimeter-Wave Limb-Emission Sounder (SMILES), *J. Geophys. Res. Atmos.*, 115, D23306, doi:10.1029/2010JD014379, 2010.
- Krankowsky, D., Lämmerzahl, P., Mauersberger, K., Janssen, C., Tuzson, B., and Röckmann, T.: Stratospheric ozone isotope fractionations derived from collected samples, *J. Geophys. Res. Atmos.*, 112, D08301, doi:10.1029/2006JD007855, 2007.
- Liang, M.-C., Irion, F. W., Weibel, J. D., Miller, C. E., Blake, G. A., and Jung, Y. L.: Isotopic composition of stratospheric ozone, *J. Geophys. Res. Atmos.*, 111, D02302, doi:10.1029/2005JD006342, 2006.
- Lyons, J. R.: Transfer of mass-independent fractionation in ozone to other oxygen-containing radicals in the atmosphere, *Geophys. Res. Lett.*, 28, 3231–3234, doi:10.1029/2000GL012791, 2001.
- Marquardt, D. W.: An algorithm for least-squares estimation of nonlinear parameters, *J. Soc. Industr. Appl. Math.*, 11, 431–441, doi:10.1137/0111030, 1963.
- Mauersberger, K.: Measurement of heavy ozone in the stratosphere, *Geophys. Res. Lett.*, 8, 935–937, doi:10.1029/GL008i008p00935, 1981.
- Mauersberger, K., Lämmerzahl, P., Krankowsky, D.: Stratospheric ozone isotope enrichments -revisited, *Geophys. Res. Lett.*, 28, 3155–3158, doi:10.1029/2001GL013439, 2001.
- Mizobuchi, S., Kikuchi, K., Ochiai, S., Nishibori, T., Sano, T., Tamaki, K., and Ozeki, H.: In-orbit measurement of the aos (acousto-optical spectrometer) response using frequency comb signals, *IEEE J. Sel. Top. Appl.*, 5, 977–983, 2012.
- Morton, J., Barnes, J., Schueler, B., and Mauersberger, K.: Laboratory studies of heavy ozone, *J. Geophys. Res.*, 95, 901–907, doi:10.1029/JD095iD01p00901, 1990.
- Ochiai, S., Kikuchi, K., Nishibori, T., and Manabe, T.: Gain nonlinearity calibration of submillimeter radiometer for JEM/SMILES, *J. Sel. Topics Appl. Earth Obs. Remote Sens.*, 5, 962–969, 2012a.
- Ochiai, S., Kikuchi, K., Nishibori, T., Mizobuchi, S., and Manabe, T.: Calibration of superconducting submillimeter-wave limb-emission sounder (SMILES) on the ISS, *Proc. SPIE* 8527, 8527, 85270Q, doi:10.1117/12.977370, 2012b.
- Ochiai, S., Kikuchi, K., Nishibori, T., Manabe, T., Ozeki, H., Mizobuchi, S., and Irimajiri, Y.: Receiver performance of the superconducting submillimeter-wave limb-emission sounder (SMILES) on the international space station, *IEEE T. Geosci. Remote*, 51, 3791–3801, doi:10.1109/TGRS.2012.2227758, 2013.
- Pickett, H. M., Poynter, R. L., Cohen, E. A., Delitsky, M. L., Pearson, J. C., and Müller, H. S. P.: Submillimeter, millimeter and microwave spectral line catalog, *J. Quant. Spectrosc. Radiat. Transf.*, 60, 883–890, doi:10.1016/S0022-4073(98)00091-0, 1998.
- Rienecker, M. M., Suarez, M. J., Todling, R., Bacmeister, J., Takacs, L., Liu, H.-C., Gu, W., Sienkiewicz, M., Koster, R. D., Gelaro, R., Stajner, I., and Nielsen, J. E.: The GEOS-5 Data Assimilation System—Documentation of Versions 5.0.1, 5.1.0, and 5.2.0., Tech. Rep. NASA/TM-2008-104606, Vol. 27, National Aeronautics and Space Administration, available at: <http://mls.jpl.nasa.gov/data/datadocs.php> (last access: 8 October 2013), 2008.
- Rodgers, C. D.: Inverse methods for atmospheric sounding: theory and practice, series on atmospheric, oceanic and planetary physics, World Sci., 2, 3605–3609, 2000.
- Rothman, L. S., Gordon, I. E., Barbe, A., Benner, D. C., Bernath, P. F., Birk, M., Boudon, V., Brown, L. R., Campargue, A., Champion, J.-P., Chance, K., Coudert, L. H., Dana, V., Devi, V. M., Fally, S., Flaud, J.-M., Gamache, R. R., Goldman, A., Jacquemart, D., Kleiner, I., Lacombe, N., Lafferty, W. J., Mandin, J.-Y., Massie, S. T., Mikhailenko, S. N., Miller, C. E., Moazzen-Ahmadi, N., Naumenko, O. V., Nikitin, A. V., Orphal, J., Perevalov, V. I., Perrin, A., Predoi-Cross, A., Rinsland, C. P., Rotger, M., Šimečková, M., Smith, M. A. H., Sung, K., Tashkun, S. A., Tennyson, J., Toth, R. A., Vandaele, A. C., and Vander Auwera, J.: The HITRAN 2008 molecular spectroscopic database, *J. Quant. Spectrosc. Radiat. Transf.*, 110, 533–572, doi:10.1016/j.jqsrt.2009.02.013, 2009.
- Sagawa, H., Sato, T. O., Baron, P., Dupuy, E., Livesey, N., Urban, J., von Clarmann, T., de Lange, A., Wetzell, G., Kagawa, A., Murtagh, D., and Kasai, Y.: Comparison of SMILES ClO profiles with other satellite and balloon-based measurements, *Atmos. Meas. Tech.*, 6, 3325–3347, doi:10.5194/amt-6-3325-2013, 2013.
- Sato, T. O., Sagawa, H., Kreyling, D., Manabe, T., Ochiai, S., Kikuchi, K., Baron, P., Mendrok, J., Urban, J., Murtagh, D., Yasui, M., and Kasai, Y.: Strato-mesospheric ClO observations by SMILES: error analysis and diurnal variation, *Atmos. Meas. Tech.*, 5, 2809–2825, doi:10.5194/amt-5-2809-2012, 2012.
- Thiemens, M. H. and Jackson, T.: Production of isotopically heavy ozone by ultraviolet light photolysis of O<sub>2</sub>, *Geophys. Res. Lett.*, 14, 624–627, doi:10.1029/GL014i006p00624, 1987.
- Worden, J., Bowman, K., Noone, D., Beer, R., Clough, S., Eldering, A., Fisher, B., Goldman, A., Gunson, M., Herman, R., Kulawik, S. S., Lampel, M., Luo, M., Osterman, G., Rinsland, C., Rodgers, C., Sander, S., Shephard, M., and Worden, H.: Tropospheric Emission Spectrometer observations of the tropospheric HDO/H<sub>2</sub>O ratio: estimation approach and characterization, *J. Geophys. Res. Atmos.*, 111, D16309, doi:10.1029/2005JD006606, 2006.

## Appendix A

### Supporting information

#### A1 Introduction of cross terms in a priori covariance matrix

We implemented cross terms between the ozone isotopomers and isotopologues in a covariance matrix for the a priori state ( $\mathbf{S}_x$ ) following the retrieval of HDO/H<sub>2</sub>O ratios from the Tropospheric Emission Spectrometer (TES) observation (Worden et al., 2006). The retrieval state vector is projected from the linear scale to the log scale ( $\mathbf{x} \rightarrow \mathbf{z}$ ) as

$$\mathbf{z} = \ln(\mathbf{x}), \quad (4)$$

and then the  $^{18}\text{OOO}$  VMR state vector ( $^{18}\mathbf{z}$ ) is given by a summation of the state vectors of the O<sub>3</sub> ( $^{16}\mathbf{z}$ ) and their isotopic ratio ( $^R\mathbf{z}$ ):

$$^{18}\mathbf{z} = ^{16}\mathbf{z} + ^R\mathbf{z}, \quad ^R\mathbf{z} = \ln\left(\frac{^{18}\mathbf{x}}{^{16}\mathbf{x}}\right). \quad (A1)$$

The covariance matrix for their variations in the a priori profiles in the log scale ( $\mathbf{S}_z$ ) is given by

$$\mathbf{S}_z = \begin{pmatrix} ^{16,16}\mathbf{S}_z & ^{16,18}\mathbf{S}_z \\ ^{18,16}\mathbf{S}_z & ^{18,18}\mathbf{S}_z \end{pmatrix}, \quad (A2)$$

$$^{16,16}\mathbf{S}_z = \mathcal{E} \left[ \left( ^{16}\mathbf{z} - ^{16}\bar{\mathbf{z}} \right) \left( ^{16}\mathbf{z} - ^{16}\bar{\mathbf{z}} \right)^T \right],$$

$$^{16,18}\mathbf{S}_z = \mathcal{E} \left[ \left( ^{16}\mathbf{z} - ^{16}\bar{\mathbf{z}} \right) \left( ^{18}\mathbf{z} - ^{18}\bar{\mathbf{z}} \right)^T \right],$$

$$^{18,16}\mathbf{S}_z = \mathcal{E} \left[ \left( ^{18}\mathbf{z} - ^{18}\bar{\mathbf{z}} \right) \left( ^{16}\mathbf{z} - ^{16}\bar{\mathbf{z}} \right)^T \right],$$

$$^{18,18}\mathbf{S}_z = \mathcal{E} \left[ \left( ^{18}\mathbf{z} - ^{18}\bar{\mathbf{z}} \right) \left( ^{18}\mathbf{z} - ^{18}\bar{\mathbf{z}} \right)^T \right].$$

Here  $\mathcal{E}$  is the expectation operator and  $\bar{\mathbf{z}}$  is the mean of  $\mathbf{z}$ . By substituting Eq. (A1),  $^{16,18}\mathbf{S}_z$  in Eq. (A2) becomes  $^{16,16}\mathbf{S}_z$ , as follows:

$$\begin{aligned} ^{16,18}\mathbf{S}_z &= \mathcal{E} \left[ \left( ^{16}\mathbf{z} - ^{16}\bar{\mathbf{z}} \right) \left( ^{18}\mathbf{z} - ^{18}\bar{\mathbf{z}} \right)^T \right] \\ &= \mathcal{E} \left[ \left( ^{16}\mathbf{z} - ^{16}\bar{\mathbf{z}} \right) \left( ^{16}\mathbf{z} + ^R\mathbf{z} - ^{16}\bar{\mathbf{z}} - ^R\bar{\mathbf{z}} \right)^T \right] \\ &= \mathcal{E} \left[ \left( ^{16}\mathbf{z} - ^{16}\bar{\mathbf{z}} \right) \left( ^{16}\mathbf{z} - ^{16}\bar{\mathbf{z}} \right)^T \right] \\ &\quad + \mathcal{E} \left[ \left( ^{16}\mathbf{z} - ^{16}\bar{\mathbf{z}} \right) \left( ^R\mathbf{z} - ^R\bar{\mathbf{z}} \right)^T \right], \end{aligned} \quad (A3)$$

If we assume that  $\mathcal{E} \left[ \left( ^{16}\mathbf{z} - ^{16}\bar{\mathbf{z}} \right) \left( ^R\mathbf{z} - ^R\bar{\mathbf{z}} \right)^T \right] = 0$  (that is, the O<sub>3</sub> VMR is uncorrelated with the oxygen isotopic ratio),

$$^{16,18}\mathbf{S}_z = ^{16,16}\mathbf{S}_z. \quad (A4)$$

In the same way,  $^{18,16}\mathbf{S}_z$  becomes  $^{16,16}\mathbf{S}_z$ . Therefore,  $\mathbf{S}_z$  is given as

$$\mathbf{S}_z = \begin{pmatrix} ^{16,16}\mathbf{S}_z & ^{16,16}\mathbf{S}_z \\ ^{16,16}\mathbf{S}_z & ^{18,18}\mathbf{S}_z \end{pmatrix}. \quad (9)$$

#### A2 Error analysis for V215

We performed the quantitative error analysis for V215 using the same method as that for the V215 ClO (Sato et al., 2012). Since retrieval procedure of V215 is based on sequentially dependent retrieval steps using the limited spectral windows (see Table A1), we followed the step-by-step retrieval to estimate the errors in the VMR of O<sub>3</sub> and  $^{18}\text{OOO}$ , and  $\delta^{18}\text{OOO}$  from the model parameters (Eq. 17). The error from the spectral noise and the smoothing error were calculated using Eqs. (18) and (20), respectively.

The window setting of V215 is described as follows. In band B, the tangent height is first retrieved using the O<sub>3</sub> line at 625.371 GHz in window B-w0. Window B-w1 is set for the retrieval of the VMR of O<sub>3</sub> with the B-w0 tangent height. The retrieved O<sub>3</sub> VMR and tangent height are used as an a priori in the retrieval of the H<sup>35</sup>Cl VMR in window B-w2. The VMR of  $^{18}\text{OOO}$  is retrieved in window B-w4 using the retrieved parameters in windows B-w0, B-w1 and B-w2 as an a priori. In band C, the tangent height is retrieved by a bias correction using the ClO line at 649.45 GHz instead of the O<sub>3</sub> line. This tangent height is employed in the retrieval of the VMR of  $^{18}\text{OOO}$  in window C-w5.

The error sources in Tables 3 and 4 were taken into account in this error analysis. The uncertainties in the spectroscopic parameters were the same as the error analysis for TOROROS. As described in Sect. 2.3, the antenna response pattern ( $R_{\text{ANT}}$ ) should be widened, but this procedure was ignored in V215. This was also included in the error sources of V215. The rejection rate of the image band ( $\beta_{\text{image}}$ ) was assumed to be one in V215; thus, the error due to this assumption was also considered. The uncertainty in the AOS response function was 10 % in the error analysis for V215. The error due to the uncertainty in  $\gamma_{\text{air}}$  of the ClO line in band C was calculated for  $^{18}\text{OOO}$  VMR in window C-w5 because the tangent height used in window C-w5 is retrieved using the ClO line as mentioned above. The results of the error analysis for the systematic and random errors in the VMRs of O<sub>3</sub> and  $^{18}\text{OOO}$  and the enrichment  $\delta^{18}\text{OOO}$  of V215 are shown in Figs. A1 and A2.

#### A3 Nighttime comparison between the two retrieval algorithms

The results of the comparison study between the TOROROS and V215 algorithms for nighttime ( $\text{SZA} > 100^\circ$ ) are shown in Figs. A3 and A4 for the VMR of O<sub>3</sub>, the VMR of  $^{18}\text{OOO}$  and  $\delta^{18}\text{OOO}$ . They showed similar behaviors as those during daytime.

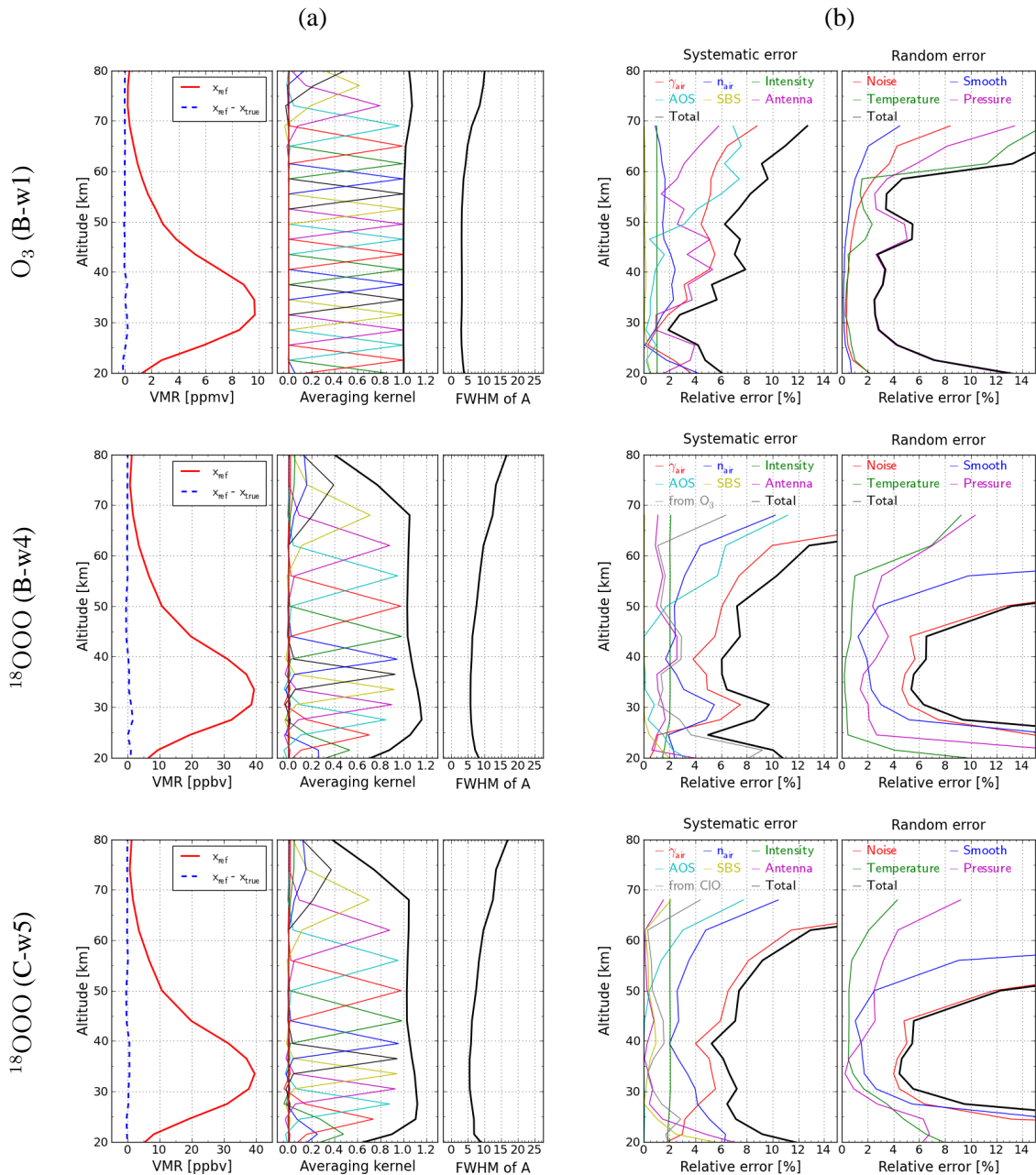


**Fig. A1.** Same as Fig. 2 but for the  $\text{O}_3$  in B-w1 (top),  $^{18}\text{OOO}$  in B-w4 (middle) and  $^{18}\text{OOO}$  in C-w5 (bottom) of V215.

#### A4 Error analysis for temperature retrieved by TOROROS

We estimated the systematic and random errors in the temperature retrieved in window b0 of TOROROS. The method and error sources considered in this analysis were the same as the error analysis for the VMR of  $\text{O}_3$  in window b1. The left panel of Fig. A5 shows the reference profile and the averaging kernel for the b0 temperature. The measurement response was larger than 0.9 in the altitude range between 20 and 57 km. The total systematic and random errors in the

temperature were about 1–2 % in the stratosphere. The uncertainty in the  $\gamma_{\text{air}}$  of the  $\text{O}_3$  line contributed more than 90 % of the total systematic error. The AOS response function had a larger contribution at altitudes above 50 km. For the random error, the pressure profiles were the dominant source for all altitudes considered in this study. The temperature profile became more important above 50 km.

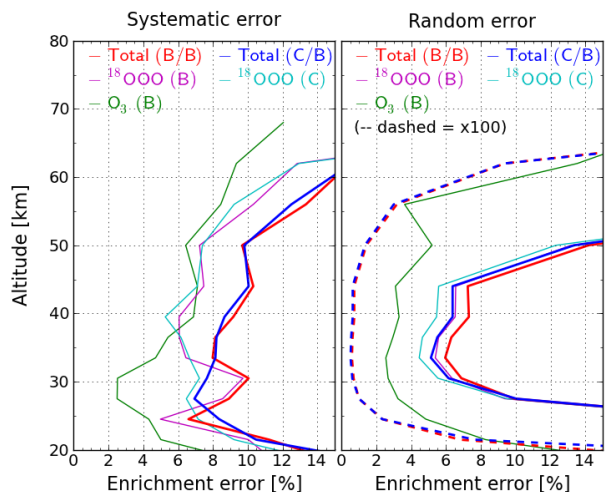


Fig. A2. Same as Fig. 3 but for V215.

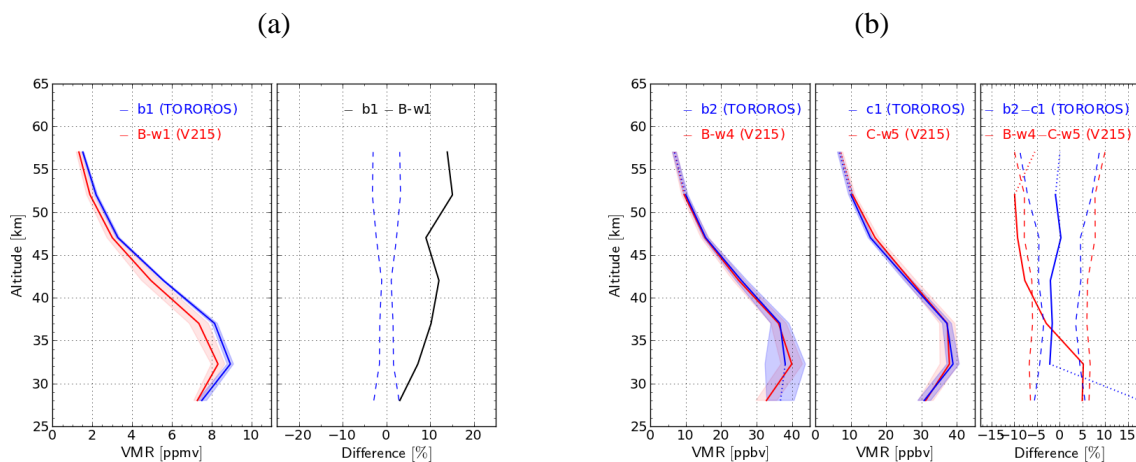


Fig. A3. Same as Fig. 4 but for nighttime.

Table A1. Spectral windows of V215.

Window / band	Frequency range	Target	Altitude range	Corresponding window in TOROROS
B-w0/band B	625.042–625.612 GHz	Tangent height	18–70 km	–
B-w1/band B	625.042–625.612 GHz	O <sub>3</sub> , temperature	18–100 km	b1
B-w2/band B	625.714–626.264 GHz	H <sup>35</sup> Cl, O <sup>17</sup> O	16–100 km	–
B-w4/band B	625.500–625.830 GHz	<sup>18</sup> O <sup>18</sup> O, O <sup>17</sup> O, HO <sub>2</sub>	20–90 km	b2
C-w0/band C	649.120–650.320 GHz	Tangent height	11–40 km	–
C-w5/band C	649.000–649.300 GHz	<sup>18</sup> O <sup>18</sup> O, <sup>17</sup> O <sup>18</sup> O	25–60 km	c1

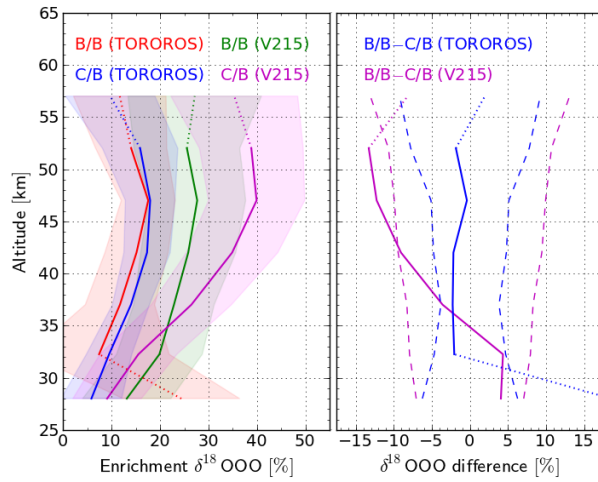


Fig. A4. Same as Fig. 5 but for nighttime.

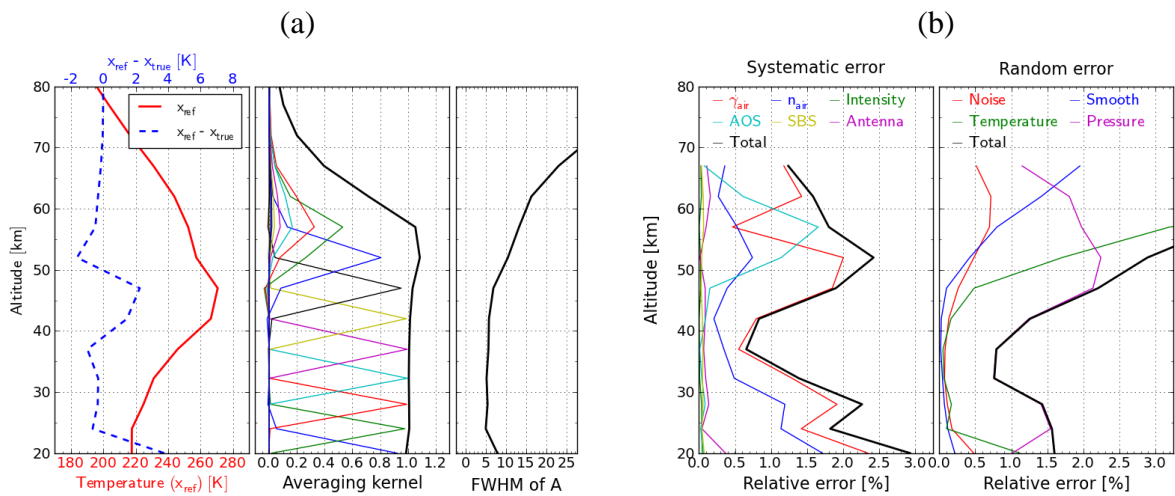


Fig. A5. Same as Fig. 2 but for the temperature retrieved in window b0. In the panel, to display the reference temperature profile ( $x_{\text{ref}}$ ), the scale of  $x_{\text{ref}}$  and the difference ( $x_{\text{ref}} - x_{\text{true}}$ ) are shown in the lower and upper x axis, respectively.